

Coseismic Slip and Afterslip of the Great M_w 9.15 Sumatra–Andaman Earthquake of 2004

by Mohamed Chlieh, Jean-Philippe Avouac, Vala Hjorleifsdottir, Teh-Ru Alex Song, Chen Ji,*
Kerry Sieh, Anthony Sladen, Helene Hebert, Linette Prawirodirdjo, Yehuda Bock, and John Galetzka

Abstract We determine coseismic and the first-month postseismic deformation associated with the Sumatra–Andaman earthquake of 26 December 2004 from near-field Global Positioning System (GPS) surveys in northwestern Sumatra and along the Nicobar–Andaman islands, continuous and campaign GPS measurements from Thailand and Malaysia, and *in situ* and remotely sensed observations of the vertical motion of coral reefs. The coseismic model shows that the Sunda subduction megathrust ruptured over a distance of about 1500 km and a width of less than 150 km, releasing a total moment of $6.7\text{--}7.0 \times 10^{22}$ N m, equivalent to a magnitude $M_w \sim 9.15$. The latitudinal distribution of released moment in our model has three distinct peaks at about 4° N, 7° N, and 9° N, which compares well to the latitudinal variations seen in the seismic inversion and of the analysis of radiated T waves. Our coseismic model is also consistent with interpretation of normal modes and with the amplitude of very-long-period surface waves. The tsunami predicted from this model fits relatively well the altimetric measurements made by the JASON and TOPEX satellites. Neither slow nor delayed slip is needed to explain the normal modes and the tsunami wave. The near-field geodetic data that encompass both coseismic deformation and up to 40 days of postseismic deformation require that slip must have continued on the plate interface after the 500-sec-long seismic rupture. The postseismic geodetic moment of about 2.4×10^{22} N m ($M_w \sim 8.8$) is equal to about $30 \pm 5\%$ of the coseismic moment release. Evolution of postseismic deformation is consistent with rate-strengthening frictional afterslip.

Online material: Summary of geodetic data used in this study.

Introduction

The characteristics of the great Sumatra–Andaman earthquake of 26 December 2004 have been only partially described by purely seismological methods. The interference between direct and reflected waves caused by the exceptionally long duration of the rupture have made it difficult to constrain the source characteristics from the analysis of teleseismic body waves. Better constraints on the seismic source have been obtained from less conventional approaches. In particular, analyses of normal modes, very-long-period waveforms, high-frequency diffracted seismic waves, or hydroacoustic waves have proven helpful (Ammon *et al.*, 2005; de Groot-Hedlin, 2005; Guilbert *et al.*, 2005; Ishii *et al.*, 2005; Krüger and Ohrnberger, 2005; Lay *et al.*, 2005; Ni *et al.*, 2005; Stein and Okal, 2005; Tsai *et al.*, 2005; Bilek,

2007). From these studies it is now clear that completion of the seismic rupture took about 515 sec, the longest ever recorded, and that rupture extended along the trench 1200 to 1500 km from northern Sumatra to the northern Andaman Islands consistent with the aftershock distribution (Bilham *et al.*, 2005; Dewey *et al.*, 2007). Uncertainty in the rupture length is due to inherent trades-offs among model parameters and to uncertainties in the data used in these studies.

Other first-order characteristics of this earthquake, such as the moment magnitude of the seismic source, the slip distribution, and the respective contribution of seismic and aseismic slip to the tsunamigenic source remain poorly constrained by these methods. For example, seismological estimates of the coseismic moment magnitude, M_w , range between 9.1 and 9.3 (Ammon *et al.*, 2005; Park *et al.*, 2005; Stein and Okal, 2005; Vallée, 2007). The variability is essentially due to different assumptions about the fault geometry.

*Present address: Department of Earth Science, University of California, Santa Barbara, California 93106.

Unusually large surface displacements accompanied the Sumatra–Andaman earthquake, making geodetic measurements particularly valuable in determining its characteristics. The displacements have been documented and modeled by a variety of techniques, including field measurements of uplifted or subsided coral heads (Bilham *et al.*, 2005; Meltzner *et al.*, 2006; Subarya *et al.*, 2006), continuous and campaign Global Positioning System (GPS) measurements (Banerjee *et al.*, 2005; Jade *et al.*, 2005; Vigny *et al.*, 2005; Gahalaut *et al.*, 2006; Subarya *et al.*, 2006), and remote sensing measurements of uplift or subsidence using optical or Synthetic Aperture Radar (SAR) images (Meltzner *et al.*, 2006; Subarya *et al.*, 2006; Tobita *et al.*, 2006). The geodetic data collected and compiled by Subarya *et al.* (2006) require a source corresponding to a released moment of 8.8×10^{22} N m, equivalent to a magnitude of M_w 9.22. This value exceeds by 30% the seismically released moment, estimated to 6.5×10^{22} N m (Ammon *et al.*, 2005; Lay *et al.*, 2005) because the geodetic surface displacements include both the coseismic deformation and about 1–2 months of postseismic deformation. In addition, Subarya *et al.* (2006) found that the seismically released moment and the slip distribution proposed by Ammon *et al.* (2005) was consistent with the coseismic displacements during the first day following the mainshock measured at continuous GPS stations in the far field in Malaysia and Thailand (Vigny *et al.*, 2005). These findings imply that a large fraction of aseismic afterslip must have occurred over the first months following the mainshock, increasing the seismically released moment by about 30%, or even more in the Nicobar and Andaman Islands area.

So far, no model adequately reconciles the tsunamigenic source, the seismological data, and the geodetic data. A reasonable fit to the satellite altimetric measurements of the tsunami (Gower, 2005) and tide gauge measurements (Merrifield *et al.*, 2005) can be obtained for sources with rupture lengths between 800 and 1400 km and moment magnitudes within the range of 9.1 to 9.3 (Lay *et al.*, 2005; Titov *et al.*, 2005; Fujii and Satake, 2007). It is not clear whether the tsunami source requires more moment than what was released during the seismic phase. Some additional aseismic slip may indeed have contributed, as suggested by Bilham (2005) and Lay *et al.* (2005), although it is now clear that this was suggested because of the tide gauge record from Port Blair, which had a clock error of 46 min (Neetu *et al.*, 2005).

This study aims to provide a better understanding of the coseismic slip distribution and postseismic afterslip of the 2004 Sumatra–Andaman earthquake using a more comprehensive set of geodetic data that have become available. In addition to data compiled in Subarya *et al.* (2006), we include new geodetic data from the Nicobar and Andaman islands (Gahalaut *et al.*, 2006) and displacements in Thailand and Malaysia (Vigny *et al.*, 2005) in our analysis. The geodetic data vary in their resolution, spatial distribution, and temporal coverage, but their different characters help to refine our understanding of this giant earthquake. We first in-

troduce the seismotectonic setting of the earthquake. We then present the geodetic data and the method used to discriminate postseismic and coseismic deformation. Next, we propose a model of coseismic slip distribution for which we test for consistency with normal modes, very-long-period surface waves, displacements recorded by the International GNSS Service (IGS) network over 1100 km from the source, and altimetric measurements of the tsunami. Finally, we use that information to constrain the distribution and evolution of afterslip, which appears to be the major contribution to postseismic deformation captured by the geodetic data analyzed in this study.

Seismotectonic Setting

The great Sumatra–Andaman earthquake occurred along the Sunda–Andaman subduction zone, which absorbs the northeastward motion of the Indian and Australian plates relative to the Sunda Shelf (Fig. 1). Along the Java Trench to the southeast of Sumatra, the Australian plate subducts beneath the Sunda Shelf in a direction nearly orthogonal to the trench and at a rate of about 63 mm/yr (Michel *et al.*, 2001; Bock *et al.*, 2003). Along Sumatra the direction of convergence becomes increasingly oblique toward the northwest and the relative plate slip is partitioned into nearly perpendicular thrusting at the trench and trench-parallel, right-lateral slip at the Sumatran fault (SF) (Fitch, 1972). The convergence rate is about 45 mm/yr and the slip rate on the Sumatran fault is 11 to 28 mm/yr (Genrich *et al.*, 2000; McCaffrey *et al.*, 2000; Prawirodirdjo *et al.*, 2000; Sieh and Natawidjaja, 2000). In the epicentral area of the December 2004 rupture, the slip rate normal to the trench is about 40 mm/yr (Bettinelli *et al.*, 2006; Socquet *et al.*, 2006). The convergence rate decreases northward as the azimuth of the trench becomes nearly parallel to the direction of motion of the Indian Plate relative to the Sunda Shelf (Fig. 1). The relative motion between India and Sunda at the latitude of the Andaman Islands is partitioned in a relatively complex way into a component of convergence across the subduction zone, possibly right-lateral slip along the Andaman fault, and extension and strike-slip faulting within the Andaman Sea (Curry, 2005). Because of poorly constrained rates and directions of extension in the Andaman Sea, the convergence rate across the subduction zone is poorly known in the region north of about 8° N. Sparse geodetic data suggest a value between 14 and 34 mm/yr (Paul *et al.*, 2001; Curry, 2005; Gahalaut *et al.*, 2006).

The Sumatra–Andaman subduction zone is thus characterized by gradual lateral variations of the convergence rate and obliquity. Other characteristics varying significantly along the trench may influence the seismic behavior and the mechanical properties of the subduction interface, the thermal regime of the subduction zone, and the force balance at the plate boundary. One variable is the age of the seafloor, which increases from about 50 Ma in the epicentral area to about 80 Ma offshore the Andaman Islands (Fig. 1). Another

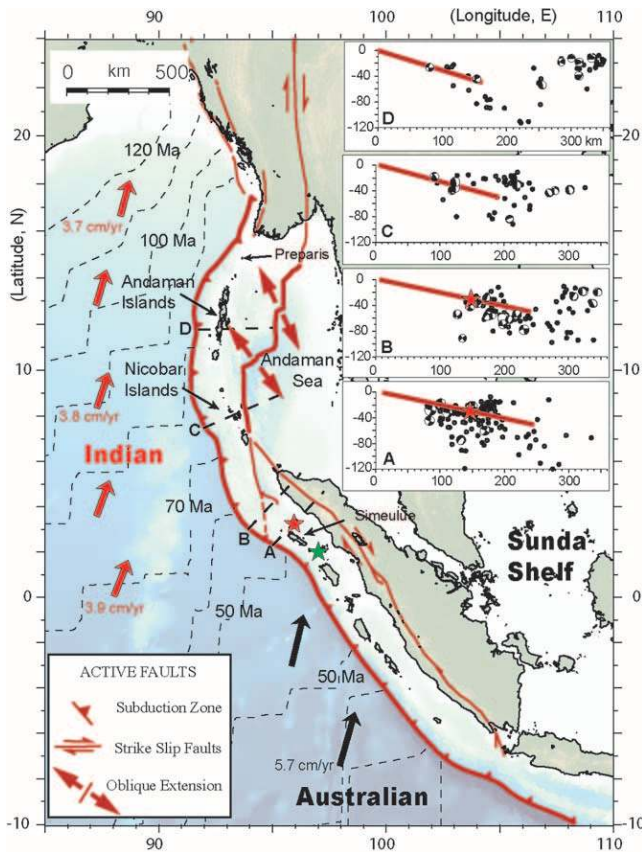


Figure 1. Neotectonic setting of the great Sumatra–Andaman earthquake. Plate velocities of Australia (~ 5.7 cm/yr) and India (~ 3.8 cm/yr) relative to Sunda were computed from the regional kinematic model of Bock *et al.* (2003) and Socquet *et al.* (2006). Age of the sea floor (Gradstein *et al.*, 1994; Cande and Kent, 1995) increases northward from about 50 Ma in the epicentral area to 90 Ma near Andaman Islands. Insets show cross sections with models' geometries, relocated seismicity (Engdahl *et al.*, 1998) between 1964 and 2002 and Harvard CMT solutions for background seismicity ($M_w > 6$) between 1973 and 25 December 2004. The stars north and south of Simeulue Island show, respectively, the epicenter of the 26 December 2004 Sumatra–Andaman earthquake and the epicenter of the 28 March 2005 Nias earthquake.

variable is the thickness of terrigenous sediments deposited on the subducting plate, which increases northward toward the apex of the Bengal fan from about 2 km to about 6 km (Fig. 2).

The subduction zone beneath Sumatra has generated several large earthquakes in the past two centuries (Fig. 2). The Nias segment, located between Simeulue Island and the Batu Islands, broke in 1861 ($M_w \sim 8.5$) (Newcomb and McCann, 1987) and again during the M_w 8.6 28 March 2005 event (Briggs *et al.*, 2006; Hsu *et al.*, 2006; Kreemer *et al.*, 2006b; Konca *et al.*, 2007). The Batu Islands segment near the Equator, where the Investigator Fracture Ridge enters

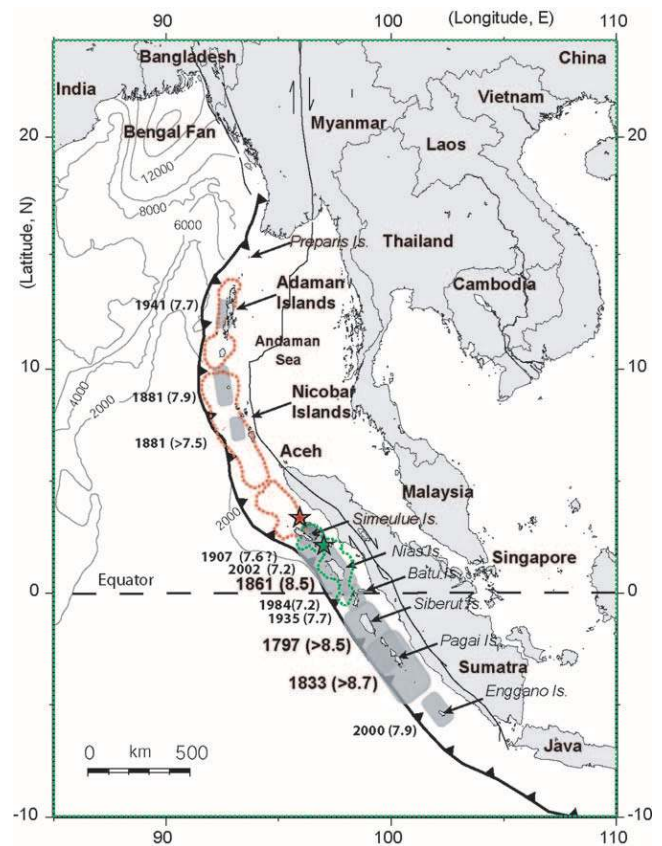


Figure 2. Historical large earthquakes of the Sunda megathrust and thickness of subducting sediment. Grey patches are the estimated ruptured areas of the major megathrust earthquakes between 1797 and 2004 (Newcomb and McCann, 1987; Ortiz and Bilham, 2003; Sieh *et al.*, 2004; Bilham *et al.*, 2005; Natawidjaja *et al.*, 2006). Contours of the sediment thickness are each 2000 m. Dotted contours are, respectively, the coseismic slip areas of the December 2004 earthquake (this study) and the March 2005 earthquake (Hsu *et al.*, 2006).

the subduction zone, has produced only moderate interplate events with magnitude less than 7.7 (Rivera *et al.*, 2002; Natawidjaja *et al.*, 2004). South of the equator, beneath the Mentawai Islands, a couplet with magnitudes estimated at $M_w \sim 8.5$ – 9.0 occurred in 1797 and 1833 (Zachariassen *et al.*, 1999; Sieh *et al.*, 2004; Natawidjaja *et al.*, 2006). In contrast, there is no historical record of any earthquakes with $M_w > 8$ from the subduction zone between Sumatra and Myanmar. Only relatively small earthquakes, with magnitudes between about 7.5 and 7.9 have occurred (Ortiz and Bilham, 2003; Bilham *et al.* 2005).

Characteristics of the Sumatra–Andaman Earthquake Derived from Seismology

Analyses of high-frequency seismic records obtained from the Global Seismic Network (Ni *et al.*, 2005), from the

Hi-Net seismic array in Japan (Ishii *et al.*, 2005), and from the German Regional Seismic Network (Krüger and Ohrnberger, 2005) indicate that the rupture took about 500 sec to propagate about 1250 km northward from the epicentral area to the northern Andaman Islands. From the analysis of T waves recorded by a hydroacoustic array at Diego Garcia in the Indian Ocean and seismic measurements from a mini-seismic array in Thailand (Guilbert *et al.*, 2005) found that the rupture lasted for 515 sec and propagated more than 1200 km, to about 14° N at the northern end of the Andaman Islands. This analysis also shows that the rupture velocity decreased from about 2.7 km/sec offshore northern Sumatra and the Nicobar Islands to 2 km/sec along the Andaman Islands.

A comprehensive view of the slip history and distribution was obtained by combining information from the body waves and surface waves with periods up to 500 sec (model III of Ammon *et al.* [2005], hereafter called Ammon-III). According to this model, the seismic moment of the earthquake is 6.5×10^{22} N m, released mostly between latitudes 2° N and 10° N. The corresponding moment magnitude is M_w 9.12. Free oscillations of the Earth generated by the earthquake indicate that the seismic phase may in fact have released even more moment beyond the 500-sec duration of the Ammon-III source model. The total moment released during the coseismic phase could have been as large as 1.1×10^{23} N m, corresponding to a moment magnitude M_w 9.3 (Stein and Okal, 2005).

Geodetic Data

The geodetic data used to derive the slip models presented in the next section are listed (E) in the electronic edition of BSSA. We distinguish:

- Near-field data, from sites less than about 300 km from the trench. These provide useful information on slip distribution and include variable amounts of postseismic deformation.
- Far-field data, mainly from continuous GPS stations, 300–1100 km from the source, where the signal is well above the noise level on daily solutions. The far-field data only marginally contribute to our knowledge of the slip distribution but are useful in constraining the total moment released during the coseismic and postseismic phases.
- Very-far-field data, mostly come from the analysis of daily time series from IGS stations more than 1100 km from the source.

Near-Field Data

Near-field observations consist of GPS survey-mode measurements in Sumatra and from the Nicobar–Andaman islands (Gahalaut *et al.*, 2006; Subarya *et al.*, 2006) (E Tables 1 and 2 in the electronic edition of BSSA). In northern Sumatra, 23 campaign GPS measurements were collected be-

tween 28 January and 19 February 2005 (Subarya *et al.*, 2006). These data were compared with campaign measurements from 1991 to 2001 (Bock *et al.*, 2003) and corrected for interseismic deformation (Subarya *et al.*, 2006).

In the Nicobar–Andaman islands, measurements at five sites were first released by the CESS (Centre for Earth Science Studies, Trivandrum, India) and incorporated in Subarya *et al.*, 2006. Refined determination of the displacements at these five sites published together with new measurements at eight sites (Gahalaut *et al.*, 2006) show small differences from those released by the CESS (Fig. 3). These data provide better spatial coverage of the Nicobar–Andaman sections and have smaller uncertainties (E Table 2 in the electronic edition of BSSA). These displacements were determined from the comparison of GPS campaign measurements at Car Nicobar, surveyed between September 2003 and February 2005 from Jade *et al.* (2005) and 12 sites measured during February and March 2004 and resurveyed between 11 and 22 January 2005 (Gahalaut *et al.*, 2006). Given the slow convergence rate and the short time between the pre-earthquake survey and the occurrence of the earthquake, we did not apply any correction for interseismic strain to these data.

Continuous GPS data were also available from the Sumatran GPS Array (SuGAR) of Caltech's Tectonics Observatory (www.tectonics.caltech.edu/sumatra/data.html), located more than 300 km south of the earthquake rupture. These data show coseismic displacements, over the first day, typically less than 1 cm, with no resolvable postseismic transient.

Coral reefs also provide valuable near-field data. Vertical displacements were measured *in situ* from the uplift or subsidence of coral heads on 17 and 18 January and on 5 February on Simeulue Island about 50 km south of the epicenter location (Subarya *et al.*, 2006). Field estimates of coastal uplift of the Nicobar and Andaman islands reported by Bilham *et al.* (2005) were also used (E Tables 6 and 7 in the electronic edition of BSSA).

We also use estimates of vertical displacement derived from remote sensing using optical images (ASTER, SPOT, and IKONOS) (Meltzner *et al.*, 2006). Except at a few sites, the remote sensing observations place only lower bounds on the amount of subsidence or uplift. They do, however, place very useful constraints on the position of the pivot line, defined as the line with no net elevation change between the uplifted area closer to the trench and the subsided area farther from the trench. The location of the pivot line constrains the width of the ruptured area. In the present study, as in model A of Subarya *et al.* (2006), we take into account a set of points along the pivot line (E Table 8 in the electronic edition of BSSA).

The near-field data indicate dominantly trenchward horizontal displacements of the sites on the islands above the subduction zone with values exceeding 5 m off the coast of northern Sumatra and in the Nicobar Islands (E Figure 3, Tables 1 and 2 in the electronic edition of BSSA). Horizontal

Table 1
Fault Geometry of the Three Rectangular Dislocations Used for the Seismological Slip Model
Ammon-III (Ammon *et al.*, 2005) and Also Used in This Study

Segment	Location of Southwest Corner		Length (km)	Strike (°)	Dip (°)
	Long. (°)	Lat. (°)			
1	95.25	1.85	280	315	12
2	93.34	3.76	680	342	15
3	91.46	9.59	480	5	17.5

Table 2
Earth Structure Parameters of the Six Superficial Layers
Based on CRUST2.0

Thickness (km)	V_s (km/sec)	V_p (km/sec)	Density (kg/m ³)
1.7	2.500	5.000	2.6000
2.3	3.650	6.600	2.9000
2.5	3.900	7.100	3.0500
196	4.473	8.080	3.3754
36	4.657	8.594	3.4465
108	4.707	4.707	3.4895

displacement decreases gradually away from the trench. Sites within 150 km of the trench rose as much as 2 m (2.09 m at Salaut island [Subarya *et al.*, 2006]) and subsided farther away from the trench (as much as 2.85 m at Teresa Island [Gahalaut *et al.*, 2006]). The position of the pivot line inferred from all measurements of vertical displacement is everywhere less than 150 km from the trench (Meltzner *et al.*, 2006). The region of uplift also shows that fault rupture extended from northern Simeulue to Preparis Island ($\sim 15^\circ$ N) over a distance of more than 1500 km, if measured along the accurate shape of the trench (Meltzner *et al.*, 2006).

Far-Field (300–1100 km from the Source) Data

Continuous GPS stations in Thailand and Malaysia, less than 1100 km from the source yield time series with a clear offset at the time of the earthquake well above the noise level (Vigny *et al.*, 2005). These records show that at all the sites the coseismic offset occurred within about 10 min of rupture initiation, contradicting the hypothesis of a silent slip event (Bilham, 2005; Bilham *et al.*, 2005). In the present study, we use the coseismic displacements as proposed by Vigny *et al.* (2005) (® reported in Table 3 in the electronic edition of BSSA) to constrain the coseismic phase. These displacements were averaged over 5 days before and after the Sumatra–Andaman earthquake to reduce the noise level at these stations (hereafter called 1-day coseismic data for simplicity). Altogether we have included in our analysis 39 far-field measurements (33 at continuous GPS sites and 6 campaign-mode measurements corrected for postseismic deformation). The maximum coseismic displacement among these data is 27 cm, at Phuket, about 500 km from the epicenter. The stations in Bangkok and Singapore, both about

1000 km from the epicentral area and at the latitudes of the northern and southern limits of the rupture, moved 7.8 cm and 2 cm, respectively (Fig. 3).

Very-Far-Field (>1100 km from the Source) Data

Many more-distant IGS stations throughout southeast Asia recorded a measurable coseismic signal (Banerjee *et al.*, 2005, 2007; Catherine *et al.*, 2005; Hashimoto *et al.*, 2006; Kreemer *et al.*, 2006a; Ohta *et al.*, 2006; Vigny *et al.*, 2005). Stations as far as 3000 km from the epicenter moved as much as 1–2 cm. We distinguish between far-field and very-far-field data because the effect of the sphericity becomes significant typically beyond about 1100 km (Banerjee *et al.*, 2005). We compared the displacements for a point source in a layered elastic half-space of moment magnitude M_w 9.1 as used in our inversion procedure with those computed using the spectral element method (SEM) with a spherical 3D earth model (Komatitsch and Tromp, 2002a). The models differ by less than 5% at all points in the near-field and far-field range. We are confident, therefore, that the model derived from the inversion of the near-field and far-field data is not significantly biased because of the 1D approximation. Displacements in the very far field were used only to check *a posteriori* our coseismic model from a forward SEM computation. For consistency with the far-field data used to derive the coseismic slip model, we considered the 53 GPS measurements reported by Vigny *et al.* (2005).

Postseismic Data

The GPS survey mode data include the combined effects of coseismic and postseismic deformation. The measurements from the Nicobar–Andaman area reported by Gahalaut *et al.* (2006) include about 20 days of postseismic displacements, whereas those reported by Subarya *et al.* (2006) for the sites near Aceh include up to 40 days of postseismic displacements. We also use far-field postseismic displacements measured within 5 days from the event (Vigny *et al.*, 2005) (® Table 4 in the electronic edition of BSSA). In this data set, postseismic displacements at 11 Thai and Malay stations exceeded 5 mm. We used the daily continuous GPS time series at Phuket (PHKT) (Vigny *et al.*, 2005), at Sampali (SAMP) (Subarya *et al.*, 2006), and at stations LEWK and UMLH of the SuGAR network deployed close to the epicentral area in the wake of the earthquake (Fig. 3). LEWK

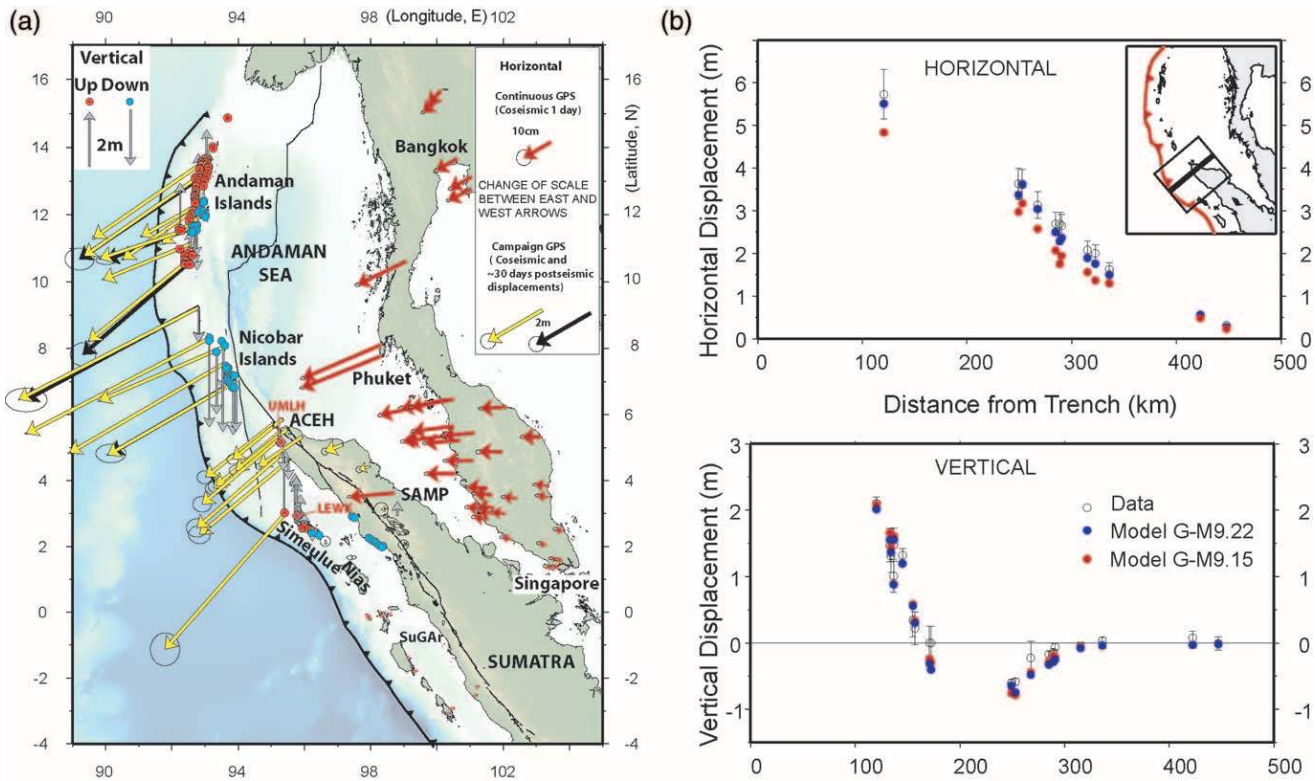


Figure 3. (Right) Summary of all near-field and far-field geodetic measurements used in this study. Dots indicate uplift and subsidence measured from satellite imagery (Meltzner *et al.*, 2006). North-pointing arrows (uplift) and south-pointing arrows (subsidence) are from field measurements using GPS, coral heads, or shoreline features (Bilham *et al.*, 2005; Gahalaut *et al.*, 2006; Subarya *et al.*, 2006). The GPS vectors that show horizontal displacements in the Nicobar–Andaman islands are from Gahalaut *et al.* (2006), in the Aceh province, Sumatra, are from Subarya *et al.* (2006). Black arrows show horizontal measurements at five sites reported by the CESS (Centre for Earth Science Studies, Trivandrum, India) that were used by Subarya *et al.* (2006). All near-field data contain about 1 month of postseismic deformation. Arrows in Thailand and Malaysia are far-field displacements that occurred during the earthquake (Vigny *et al.*, 2005). Note the change of horizontal displacement scale between arrows to the west (Andaman–Nicobar–Aceh) and arrows to the east (Thailand, Malaysia, and SAMP). (Left) Horizontal (top) and vertical (bottom) profiles of the geodetic data in the epicentral area compared with model G-M9.22 and model G-M9.15. (See Table 3 and Figs. 7 and 9 for more details.)

and UMLH began operations within 42 days and 47 days after the event, respectively. Finally, we also account for the 30 days postseismic displacements measured in Bangkok (Hashimoto *et al.*, 2006) and in Singapore (Subarya *et al.*, 2006) (Table 5 in the electronic edition of BSSA).

Modeling Approach

To better assess the consistency with seismological models, we determined best-fitting geodetic models with the same fault geometry and layered structure as in model III of Ammon *et al.* (2005). This approach allowed a straightforward comparison of the seismic moment released along strike without any biases due to geometrical and structural differences between seismological and geodetic models. The

fault geometry is quite consistent with the 3D geometry of the plate interface as delineated from relocated seismicity (Engdahl *et al.*, 1998), Harvard CMT solutions of aftershocks and background foreshocks (sections A, B, C, and D in Fig. 1). The model fault consists of three subsegments with different strikes and with dip angles increasing from 12° in the south to 17.5° in the north (Table 1). Following the methodology of Ji *et al.* (2002), the model fault comprises 20×16 km cells and Greens functions are computed using CRUST2.0 earth structure (Table 2). Computation done with the PREM earth structure showed insignificant differences. The static displacements are computed following the approach of Xie and Yao (1989).

We search for the minimum cost function, which is a combination of the weighted sum of residuals squared, χ^2 ,

Table 3
Coseismic Models Parameters and Associated χ^2

Name	Data Used	M_w	M_0 (10^{22} N m)	χ_r^2	$\chi_{r,FF}^2$	χ_{r,NF_GPS}^2	χ_{r,NF_Up}^2	Smooth
Ammon-III	seismic records*	9.12	6.50	3086	33.5	8186	1039	81
G-M9.12	GPS FF†	9.12	6.57	2509	2.07	7505	1021	35
Inversions of Near-Field Data Only by Increasing the Gahalaut <i>et al.</i> (2006) Data Uncertainties ($G*n$)‡								
G-M9.27	NF data§	9.27	10.60	533	109	929	562	48
NF_G*5	NF data	9.26	10.21	9.06	48.7	5.11	8.61	50
NF_G*10	NF data	9.24	9.52	4.90	23.5	3.16	4.61	49
NF_G*13	NF data	9.23	9.15	3.44	15	2.19	3.4	48
G-M9.22	NF data	9.22	8.95	2.96	11.3	2.23	2.76	45
Inversions of All the Geodetic Data by Increasing the Gahalaut <i>et al.</i> (2006) Data Uncertainties								
G-M9.26	all data	9.26	10.2	515	136	946	803	46
ALL_G*5	all data	9.20	8.23	24.0	20.1	35.54	60.9	51
ALL_G*10	all data	9.16	7.31	11.1	7.41	20.29	34.1	49
G-M9.15	all data	9.15	6.93	6.42	3.87	13.93	2.95	43
ALL_G*20	all data	9.14	6.63	6.33	4.03	12.38	27.4	41
ALL_G*25	all data	9.13	6.52	5.05	3.52	9.47	26.6	39
ALL_G*30	all data	9.12	6.32	4.63	3.48	8.47	26.2	41
ALL_G*40	all data	9.12	6.23	3.79	3.37	6.15	25.8	36
ALL_G*50	all data	9.11	6.12	3.31	3.42	4.72	25.6	34
Inversions of All the Geodetic Data with Gahalaut <i>et al.</i> (2006) Data Uncertainties Increased by a Factor 15 ($G*15$) and Variable Smoothness								
G-M9.16	all data	9.16	7.15	3.57	4.16	3.55	2.41	200
G-M9.15	all data	9.15	6.93	6.42	3.87	13.93	2.95	43
G-M9.13	all data	9.13	6.55	9.02	4.76	20.41	3.01	37
G-M9.10	all data	9.10	5.97	13.8	6.38	30.91	3.33	31
G-M9.06	all data	9.06	5.14	21.3	13.8	48.77	3.97	27
G-M9.05	all data	9.05	4.94	25.4	17.0	58.5	3.71	26
G-M9.02	all data	9.02	4.39	33.3	30.4	68.73	4.45	26
G-M9.01	all data	9.01	4.36	34.2	31.8	69.65	4.76	25

The χ^2 is defined as: $\chi^2 = \sum_{i=1}^n ((\text{obs}_i - \text{pred}_i)/\sigma_i)^2$, where obs is the observed measurement, pred is the prediction, and σ corresponds to the $1 - \sigma$ formal uncertainties. The reduced χ^2 is defined as: $\chi_r^2 = (\chi^2/n)$, where n is the number of data. $\chi_{r,FF}^2$ is the reduced χ^2 for the far-field data only and $\chi_{r,NF}^2$ is the reduced χ^2 for the near-field data (GPS or UP).

*Model-III from Ammon *et al.* (2005). Green's function for the inversion of the seismic/geodetic data and determination of seismic moment were computed assuming CRUST2 layered model (<http://mahli.ucsd.edu/Gabi/rem.dir/crust/crust2.html>).

†Using the coseismic displacements table proposed by Vigny *et al.* (2005).

‡ $G*n$ means that the uncertainties of Gahalaut *et al.* (2006) data were increased by a coefficient of n .

§Using the tables as proposed by Gahalaut *et al.* (2006) and Subarya *et al.* (2006).

and two other terms meant to control the smoothness and moment:

$$\text{Cost} = \chi^2 + \lambda_1(\Delta s/\alpha)^2 + \lambda_2((M_0 - M'_0)/\beta)^2 \quad (1)$$

where Δs is the average difference of slip between adjacent cells, M'_0 is some *a priori* scalar moment, meant to be a lower bound. In all inversions listed in Table 3, we applied a starting value $M'_0 = 6.5 \times 10^{22}$ N m (corresponding to M_w 9.1). The normalization coefficients α and β are determined so that for $\lambda_1 = \lambda_2 = 1$ the three criteria have equal importance, meaning that for the best-fitting model $\chi^2 = (\Delta s/\alpha)^2 = ((M_0 - M'_0)/\beta)^2 = \text{cost}/3$. The coefficient λ_1 is varied to control the smoothness of the solution and λ_2 is varied to control the weight assigned to minimize the total moment. At each nodal point, the model parameters are the rake and the amplitude of the slip vector. In the two southern segments, the rake is constrained to be $90^\circ \pm 20^\circ$ given the trench normal azimuth of the rake of most interplate earth-

quakes from the background seismicity. In the northern segment we allow the rake to vary in the range $90^\circ \pm 60^\circ$. The slip amplitude is allowed to vary by 1-m increments and is limited to a maximum value of 30 m.

The spatial resolution of the slip distribution at depth is directly related to the spatial coverage of the surface data. Checkerboard resolution reveals on which sections of the megathrust the slip is well resolved. We divided the megathrust into 140×100 km² subfaults with uniform slip set to 0 or 12 m and computed the predicted displacement at all the points where we have geodetic observations (Fig. 4a). Each checkerboard model is assigned a moment M_0 9.15×10^{22} N m, corresponding to a M_w 9.23 rupture. Resolution is relatively poor if only the far-field data are inverted (Fig. 4b). The moment is underestimated by only 3%. As expected, the resolution is significantly improved when all the geodetic data are considered (Fig. 4c). In particular, the lateral variations of the downdip slip patches are well reproduced due to the information on the near-field vertical dis-

placements. The sparse distribution of the islands makes the resolution relatively poor for the shallower patches near 4° N and 9° N. The tendency is still to underestimate the total moment by 3%. These tests show that the near-field data provide some constraints on the slip model and also show that we should be cautious regarding the interpretation of details.

Initial Modeling Results

As a starting point, we have computed the displacements predicted from the M_w 9.12 seismological slip model Ammon-III (Fig. 5). If we first focus on the comparison with coseismic displacements measured in the far field, the seismological model predicts displacements which agree well with the observed azimuths, but yields amplitudes that are too small. The reduced chi-square computed for this subset of data from Thailand and Malaysia, defined as

$$\chi_r^2 = 1/n \sum_{i=1,n} ((\text{obs}_i - \text{pred}_i)/\sigma_i)^2 \quad (2)$$

where n is the number of data in the considered subset of data and σ , the 1-sigma uncertainties, is accordingly high ($\chi_r^2 = 33$; Table 3). This shows that there is probably not enough released moment in this model to account for the

coseismic displacements measured during the first day following the earthquake. Misfits between the predicted and measured displacements are much worse in the near field. A reduced chi-square of $\chi_r^2 = 8186$ is obtained if we consider only the near-field GPS survey mode and $\chi_r^2 = 1039$ if we consider only the near-field uplift/subsidence observations. They match neither in amplitude, with predicted displacements values systematically too low, nor in direction with most of the observations in Sumatra and Nicobar–Andaman islands. The misfit might be due to both a deficit of moment in the model, an inadequate slip distribution, or fault geometry, reflecting the uncertainty inherent to the seismological inversion when no near-field geodetic data are included to help pinpoint the exact location of the main slip patches. Also the misfit to near-field data is probably partly due to postseismic deformation, a hypothesis that we pursue here.

We have first run inversions in which the far-field (FF) and near-field (NF) data are considered separately. The data are weighted according to the 1- σ uncertainty originally assigned to each datum (see tables in the electronic edition of BSSA). These tests are useful to assess whether the uncertainties are correctly scaled when the different types of data are mixed. Also they helped us to assess whether it is possible to reconcile data from different epochs after the earthquake despite the evolution of the deformation.

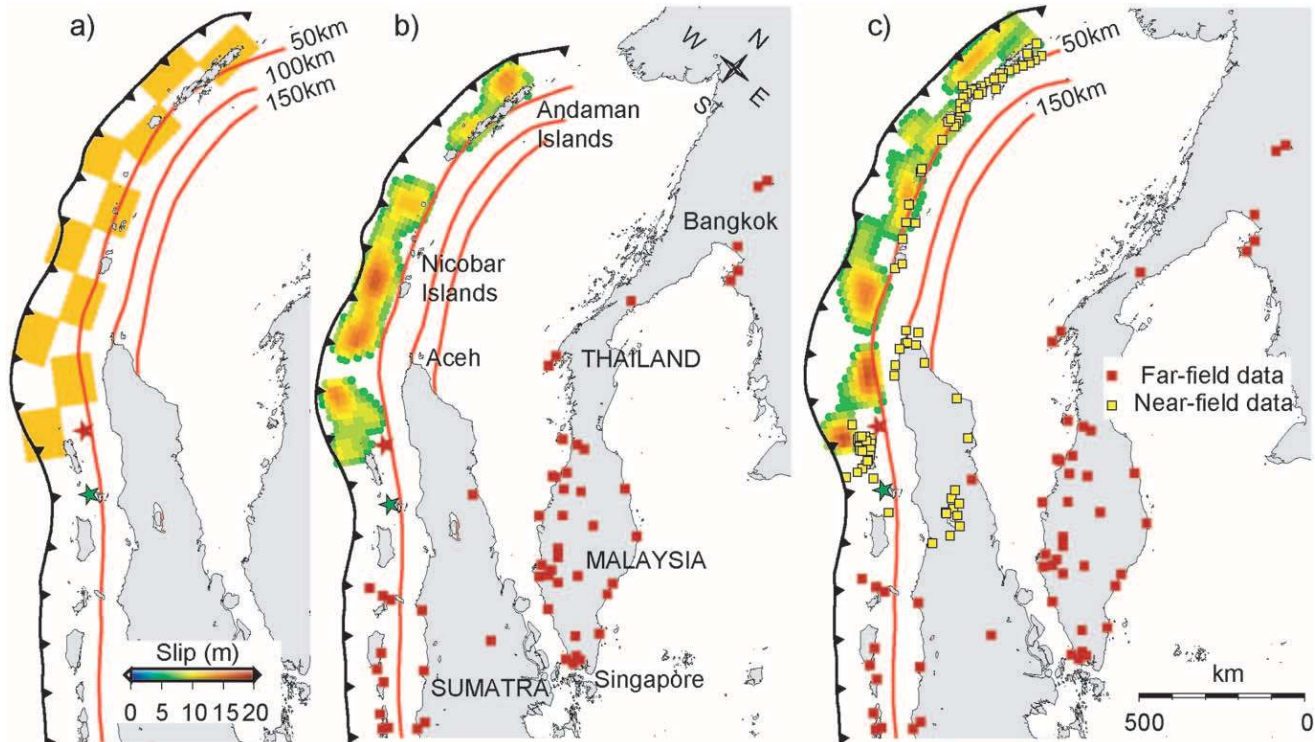


Figure 4. Checkerboard resolution tests using only far-field data (b) or both far-field and near-field data (c). Theoretical displacements at the points where we have geodetic observations were computed using the checkerboard slip distribution shown in (a) with uniform 12 m of slip on each patch. The checkerboard model (a) is assigned a moment M_0 9.15×10^{22} N m corresponding to a M_w 9.23. Slip models inversion in both (b) and (c) have a moment of M_0 8.9×10^{22} N m.

Inversion of Far-Field Data Only

If only the far-field data are considered and weighted according to the uncertainties assigned by Vigny *et al.* (2005) (© Table 3 in the electronic edition of BSSA), the inversion yields a minimum χ_r^2 of 2.07 with a moment M_0 6.57×10^{22} N m, the equivalent of a M_w 9.12 (model G-M9.12, G for geodetic, Table 3). The hypothesis that the assigned uncertainties represent $\sim 67\%$ confidence level intervals on the measurements therefore seems reasonable. Although the moment of model G-M9.12 is similar to the moment of the seismic model Ammon-III, the slip distributions are, in fact quite, different (Figs. 5 and 6). The slip distribution of model G-M9.12 is smoother but more peaked than that of the seismic model. Fault slip reaches 10–15 m in two patches, one west of Aceh and the other west of the Nicobar islands. Note that this model is different from that obtained by Vigny *et al.* (2005) who found a solution with much deeper slip patches. The main reason for the difference is

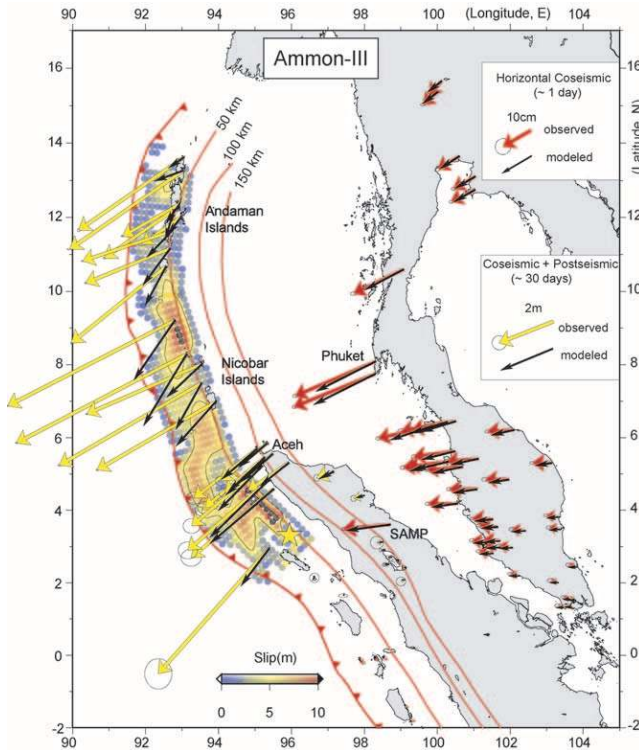


Figure 5. Predicted horizontal (black) surface displacements derived from the Ammon *et al.* (2005) model of megathrust slip (slip contours each 5 m). GPS vectors with 95% confidence ellipses are data from near-field and far-field sites. We explore the reasons for the great disparity between the geodetic data and the Ammon-III model, which was derived solely from the inversion of body waves and surface waves with periods less than 500 sec. The contours of the top of the slab (50–100–150 km) are from Gudmundsson and Sambridge (1998). Note the change of scale between arrows to the west (Andaman–Nicobar–Aceh) and arrows to the east (Thailand, Malaysia, and SAMP).

that we are using a layered half-space whereas Vigny *et al.* (2005) assumed a 1D homogeneous half-space and a shallower fault dip.

The near-field displacements predicted from model G-M9.12 are significantly smaller than the observations (Fig. 6). The χ_r^2 computed on either the horizontal displacements or the vertical displacements in the near field are always higher than 1000 (Table 3).

Inversion of Near-Field Data Only

For this inversion, we considered all the near-field data and the four GPS stations in the far field at which displacements including 30 days of postseismic deformation are known (© see Tables 1, 2, 5, 6, 7 and 8 in the electronic edition of BSSA). The best-fitting slip model corresponds to a released moment M_0 10.60×10^{22} N m (model G-M9.27; Table 3). The χ_r^2 is again unreasonably high, with values larger than 500. Our interpretation is that the data set is more heterogeneous than what the uncertainties really reflect, because of ignorance of the evolution of the deformation. In particular, the misfits of the data from the Nicobar–Andaman

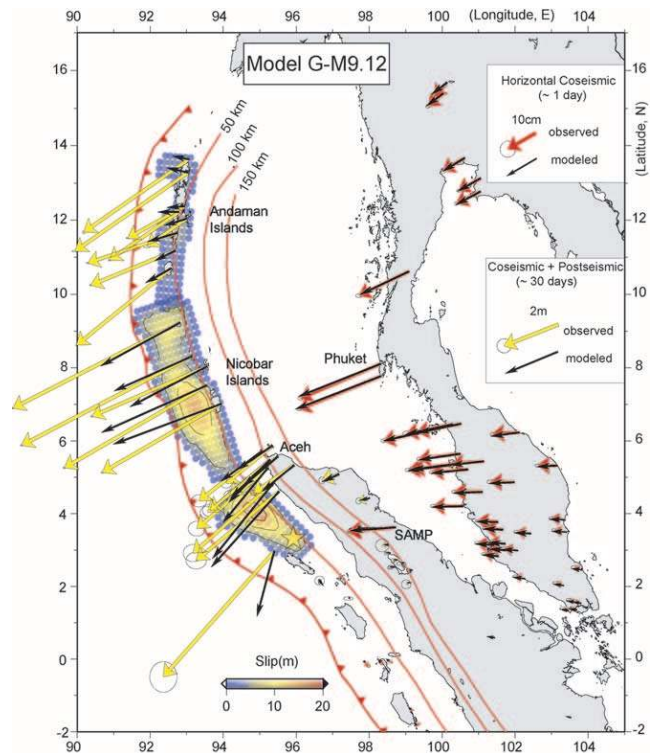


Figure 6. Dots show slip distribution of model G-M9.12 (slip contours each 5m), which was obtained just from the inversion of far-field 1-day coseismic displacements. The near-field displacements predicted from this finite source model (black vectors) are shown for comparison with the near-field measurements. The parameters of this model are listed in Table 3. Note the change of scale between arrows to the west (Andaman–Nicobar–Aceh) and arrows to the east (Thailand, Malaysia, and SAMP).

islands contribute most to the high χ_r^2 value, because of the small uncertainties initially assigned by Gahalaut *et al.* (2006). The uncertainties in the data set of Subarya *et al.* (2006) are much larger, typically by a factor of 10 or more, and therefore leave more room for misfits because all the measurements don't capture the same amount of postseismic deformation. This is why it was possible for Subarya *et al.* (2006) to find a slip model that fit these data, with a reduced chi-square of only 2.5. We considered that model to be representative of the coseismic slip plus 30 days of postseismic deformation.

To take into account the postseismic displacements included in the near-field data of the Nicobar–Andaman islands (and so to reduce the chi-square), we have rescaled the uncertainties assigned to the data of Gahalaut *et al.* (2006). We include the far-field displacements measured at the four CGPS stations in Thailand, Malaysia, and Sumatra, including the coseismic phase and 30 days of postseismic deformation. The uncertainties assigned to these four records were not rescaled, so they put relatively tight constraints on the total moment forcing the slip model to include 30 days of postseismic, although the near-field data were collected 20 to 40 days after the earthquake. The best-fitting model, G-M9.22 yields a reduced chi-square of 2.96 (Fig. 7). With this rescaling the weighted errors are relatively consistent with the assumption of a Gaussian distribution with a variance equal to 1, in accordance with inversion theory.

Model G-M9.22 yields a moment of M_0 8.95×10^{22} N m (Fig. 7), and is meant to represent the coseismic moment released by the earthquake and 30 days of postseismic deformation. This model is an updated version of model A described in Subarya *et al.* (2006). Although the total moment is the same, corresponding to M_w 9.22, the two models have slightly different slip distribution because the data of Gahalaut *et al.* (2006) require more slip beneath the Nicobar Islands than the sparser data set of the CESS. If we compare the displacements predicted at all far-field sites (in Thailand and Malaysia), the modeled azimuths of displacements fit well the azimuths of coseismic displacement, but the predicted amplitudes of about 15–20% are systematically too high, as expected given the amount of postseismic deformation included in this model. If we take Ammon-III as a reference for the coseismic phase, postseismic deformation over the first month would have increased the moment by about 30%.

Joint Inversion of Near-Field and Far-Field Data

If we invert jointly all the geodetic data, the best-fitting model yields a moment M_0 10.2×10^{22} N m (model G-M9.26) with a χ_r^2 higher than 500. This poor fit is primarily due to the impossibility of reconciling the two sets of data, confirming that postseismic displacements in the near field cannot be neglected. The model G-M9.26 is biased by the near-field data, in particular, because of the small uncertainties assigned to the data from Gahalaut *et al.* (2006).

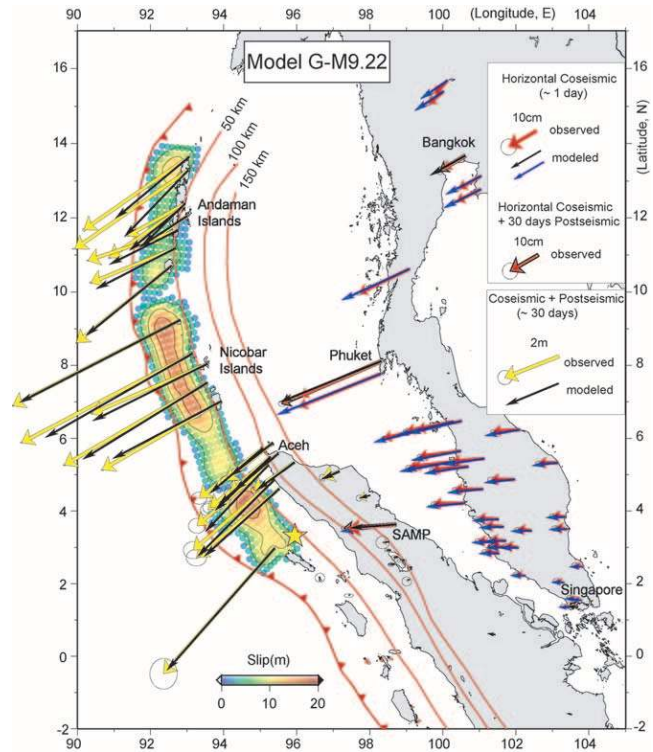


Figure 7. Slip distribution of model G-M9.22 (slip contours each 5 m), which was obtained just from the inversion of the near-field displacements and four GPS stations in the far-field Bangkok, Singapore, Phuket, and SAMP at which displacements including 30 days of postseismic deformation are known. The predicted far-field displacements from this finite-source model are larger than the actual coseismic (1-day) far-field displacements. The parameters of this model are listed in Table 3. Note the change of scale between arrows to the west (Andaman–Nicobar–Aceh) and arrows to the east (Thailand, Malaysia, and SAMP).

Coseismic Slip Model

Here we define a coseismic (1 day) slip model, taking into account the constraints provided by both the near-field and far-field data. Our strategy has been to test several models obtained from the joint inversion of the far-field and near-field data and then to select the models yielding a reasonable reduced chi-square when the predictions of models are compared to only the 1-day coseismic measurements (i.e., the far-field data from Vigny *et al.* [2005]). The fit to these data is quantified from the reduced chi-square of the far-field data, $\chi_{r,FF}^2$, computed with the originally assigned uncertainties (Table 3 in the electronic edition of BSSA).

We have considered several models obtained by varying the relative weight assigned to the near-field data of Gahalaut *et al.* (2006), or by varying the weight put on the smoothness of the solution. The relative weighting of the data of Gahalaut *et al.* (2006) and of Subarya *et al.* (2006) is the same as in model G-M9.22. All the models are listed in Table 3 and

the misfit to the far-field coseismic data $\chi^2_{r,FF}$ is reported in Figure 8. Models obtained with a low weight on the smoothness (small $\lambda 1$) yield very patchy slip models highly biased by the distribution of near-field geodetic data. A satisfying fit to the coseismic displacements is obtained for only a narrow range of M_w values (Fig. 8). If we arbitrarily select models with $\chi^2_{r,FF} < 5$, the coseismic moment release falls in the range M_0 $6.55\text{--}7.15 \times 10^{22}$ N m, corresponding to M_w 9.11 to M_w 9.16. Although we haven't tested all possible trade-offs among the model parameters, we estimate that this range of values is probably reliable at a confidence level higher than 95%.

Our preferred coseismic model, G-M9.15 (Fig. 9), was obtained from the inversion of the 1-day coseismic data together with the near-field data and by increasing the uncertainties of the Gahalaut *et al.* (2006) data by a factor of 15. The $\chi^2_{r,FF}$ is 3.87 and the displacements in the near field are systematically too small but the azimuths are well adjusted. The moment released by this model is M_0 6.93×10^{22} N m, equivalent to an M_w 9.15. Model G-M9.15 probably offers a reasonable compromise by taking into account the constraints from near-field data on the spatial distribution of slip and the constraints from far-field data on the total released moment.

The misfits between this model and near-field data probably represent primarily the amount of postseismic displacement in this data set. The misfits are largest beneath the Andaman Islands, where we found no solution that reconciles the near-field data with the far-field data. This is essentially because the far-field coseismic displacements all point toward the ruptured segment between 3° and 8° N, suggesting that most of the coseismic moment was released within this range of latitude, as shown by model G-M9.12 (Fig. 6).

Consistencies with the Latitudinal Seismic Moment Released and the T Waves

The slip distribution of model G-M9.15 is similar in its gross features to that estimated from seismological data using the same fault geometry and earth structure as the Ammon-III model (Ammon *et al.*, 2005). Figure 10 compares the latitudinal variation of the seismic moment and the geodetic moment, with uncertainties derived by propagating the rescaled uncertainties on the geodetic data. The seismic and geodetic moments have a similar pattern. The main difference appears between 7° and 10° N, the latitudes of the Nicobar Islands, where the geodetic moment is appreciably higher. This difference accounts for most of the excess moment in the geodetic model.

The latitudinal variation of geodetic moment shows three distinct peaks, at about 4° N, 7° N, and 9° N. These coincide with the latitudinal variation of the energy radiated by T waves (Fig. 10) (Guilbert *et al.*, 2005). These peaks are also consistent with the three distinct bursts of energy interpreted from records of high-frequency diffracted body waves (Ni *et al.*, 2005).

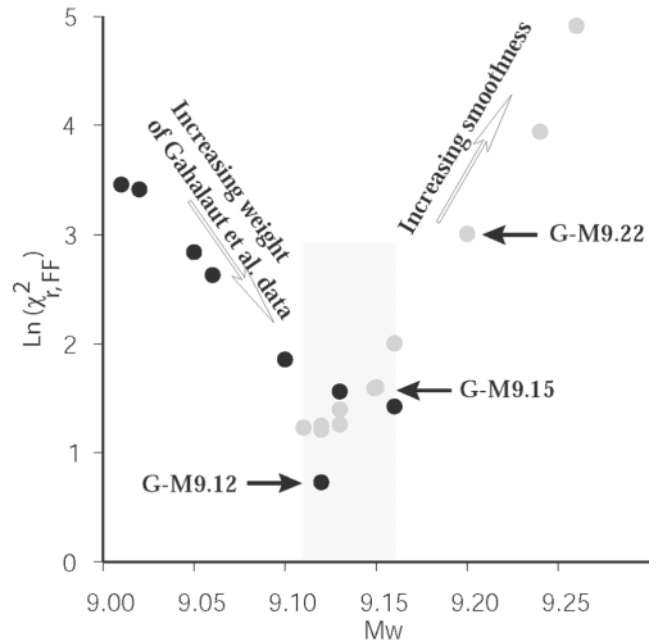


Figure 8. The chi-square of the 1-day coseismic far-field data, $\chi^2_{r,FF}$, varies as a function of M_w for the models obtained from the joint inversion of the far-field 1-day coseismic data and near-field data. The various models were obtained by varying the weight put on the near-field data (black dots) and on the smoothness of the slip model (grey dots). Model G-M9.15 is our preferred coseismic model. Details of the parameters are in Table 3.

Figure 11 shows a vector plot of the distribution of coseismic fault slip (model G-M9.15). Local rakes are nearly perpendicular to the nearby trench, except in the north, where the component of right-lateral slip is largest. For comparison with the five-sources model proposed by Tsai *et al.* (2005), we have decomposed our model into five segments and summed the seismic-moment tensor at each node within each segment. We then present the best-fitting double-couple mechanism for each subsource (Fig. 11). The rakes of these focal mechanisms deviate less than 10° from those of the CMT solutions for each subsource proposed by Tsai *et al.* (2005).

Consistency with the Normal Modes

We use very-long-period modes below 1 mHz to constrain the seismic moment and validate the slip model G-M9.15 inverted from the geodetic data. To compute the very-long-period normal modes, modal coupling caused by Earth's rotation, ellipticity and heterogeneities of earth structure are taken into account (Park and Gilbert, 1986; Dahlen and Tromp, 1998; Park *et al.*, 2005). Because inversion of geodetic data only provides static information, that is, the final slip distribution, we assume constant rise time, taken to be 20 sec, and constant rupture velocity between 2.2 and

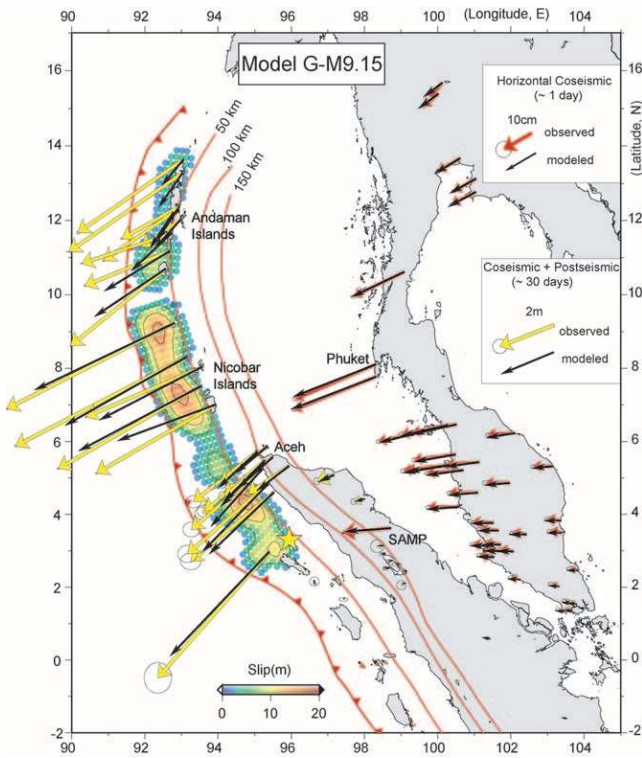


Figure 9. Slip distribution and predicted GPS displacements (black vectors) for the preferred coseismic model G-M9.15. Far-field coseismic displacements are representative of the displacements measured the day after the earthquake (Vigny *et al.*, 2005). Near-field displacements include coseismic and between 20 to 40 days of postseismic deformation. Note the change of scale between arrows to the west (Andaman–Nicobar–Aceh) and arrows to the east (Thailand, Malaysia, and SAMP).

2.6 km/sec, in agreement with average rupture velocity as proposed by seismic and hydroacoustic data (Guilbert *et al.*, 2005; Ni *et al.*, 2005). Because modal spectrum fall-off is determined by the width and shape of the moment-rate function, we find that a constant rupture velocity of 2.2 km/sec fits the spectral fall-off best (Fig. 12). Assuming a faster rupture velocity of 2.6 km/sec, we can predict the amplitude of the gravest mode ${}_0S_2$ very well but tend to overpredict the amplitude of modes near 1 mHz, because the spectral fall-off predicted by the narrower moment-rate function is too slow. Given these assumptions, we are able to explain the amplitudes of modal peaks very well with our preferred coseismic slip model (Fig. 13). This shows that there is no need of moment magnitude M_w larger than 9.15 to account for the normal mode observations. This suggests that most of the slip in the geodetic coseismic model occurred during the coseismic phase (in about 500 sec), without any need for aseismic additional slip. This is consistent with the observation that the final static displacements at the CGPS stations in Thailand and Malaysia were reached in less than 600 sec (Vigny *et al.*, 2005).

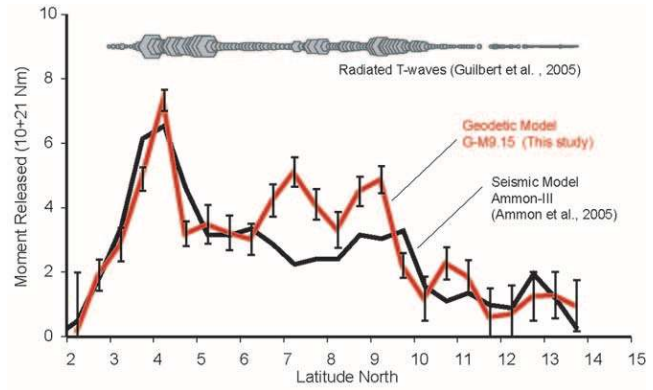


Figure 10. Latitudinal variations of scalar moments as determined from seismic model Ammon-III (Ammon *et al.*, 2005) and from the geodetic model G-M9.15. Each point represents the moment release determined from the summation of the seismic-moment tensors at all nodes in the slip model within a 0.5° -wide latitudinal bin. The error bars were estimated by propagating the uncertainties on the geodetic measurements within each latitudinal bin. Both our model and the model derived from the latitudinal variation of radiated energy by T waves (Guilbert *et al.*, 2005) show three distinct regions of energy release. The size of hexagonal symbols corresponds to the relative amplitude released since the earthquake as recorded by hydrophone sensors at Diego Garcia islands.

Consistency with Long-Period Surface Waves (<1000 sec) and Very Far-Field Displacements

To test the geodetic model with seismic and very far-field GPS measurements, we use a SEM (Komatitsch and Tromp, 2002a, 2002b) to compute synthetic waveforms. This method accurately accounts for 3D structure, ellipticity, gravity, rotation, topography, and ocean load. We use the 3D crustal model Crust 2.0 (Bassin *et al.*, 2000) and the 3D mantle model s20rts (Ritsema *et al.*, 1999). Each subfault is inserted as a separate source with the mechanism and amplitude determined by the source inversions. The timing is computed by using a fixed rupture velocity and the rise time is fixed at 20 secs for each subfault.

To simplify the comparison of the many wave forms in multiple frequency bands, we use the amplitude of the surface waves to estimate the fit. The data are deconvolved to displacement, and data and synthetics are then bandpassed using a four-pole, two-pass Butterworth filter. To estimate the amplitude we divided the data and synthetics for a given group-velocity window. We use three bandpasses (100–200, 200–500, 500–1000 sec) and corresponding group-velocity windows centered on the (3.75, 3.65, 6.2 km/sec) arrival with half-width (400, 400, 750 sec), respectively.

The amplitude ratio between data and synthetics for each station is then shown in Figure 14 as a function of azimuth. The longest-period pass band, 500–1000 sec, is

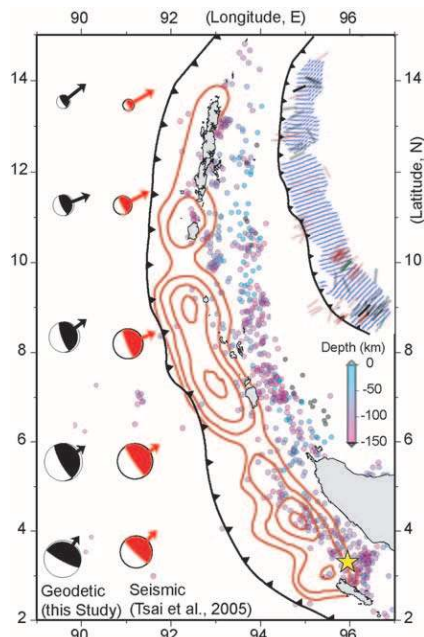


Figure 11. Summary of slip characteristics on the megathrust during the 2004 earthquake for model G-M9.15. Slip contours are each 5-m increments. Most of the 2004 coseismic slip occurred trenchward of prior seismicity (circles from Engdahl *et al.*, 1998). Black beach balls are best-fitting double-couple mechanism for five regions of the rupture for model G-M9.15. These are quite similar to the beach balls given by Tsai *et al.* (2005), based on centroid moment tensor (CMT) analysis of the earthquake. The upper inset shows the azimuth of slip on the megathrust (small arrows) which is primarily downdip south of 12° N but strike-slip farther north. Bars are the slip-vector azimuths of shallow dipping foreshocks and aftershocks from the Harvard CMT catalog.

close to the duration of the event and as such is most sensitive to the overall moment of the event, similar to the Earth's normal modes. In this pass band, the amplitude ratio between data and synthetics is close to 1 for most azimuths (Fig. 14).

The shorter-period pass bands are more sensitive to the constructive and destructive interference between waves emitted from different parts of the fault plane. The synthetics in the period range of 200–500 sec are too small to the north where the effect of constructive interference is the largest, whereas the synthetics in the shorter-period pass band of 100–200 sec are too large. Many factors contribute to the amplitude, such as the width of each patch, the separation between patches, and the assumed rupture velocity. We find that using the slip model from the geodetic inversion, the best overall match to the amplitudes for a fixed rupture velocity (VR) is obtained for VR around 2 km/sec. For a rupture speed of 2.2 km/sec the 100- to 200-sec amplitudes are underestimated by a factor of 4 in the northwest. Note that both variability in rupture velocity and probably slight adjustment

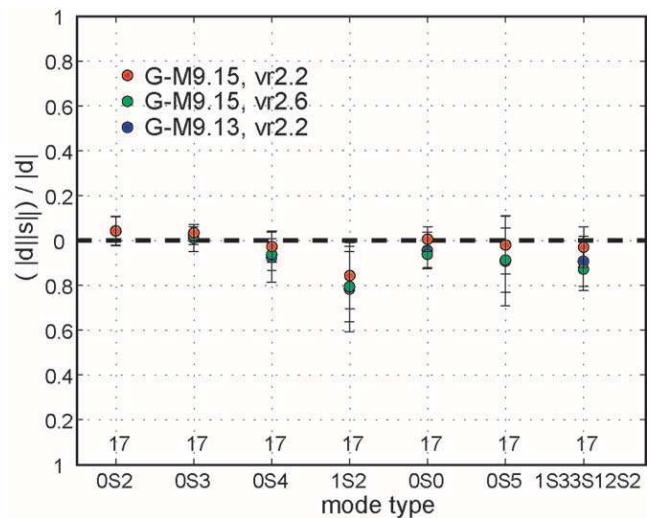


Figure 12. Misfit between data and geodetic model G-M9.15 synthetics below 1 mHz 144 hours of vertical motions are Hann-tapered before discrete Fourier transformation. Included are 17 GSN and Geoscope stations used by Park *et al.* (2005).

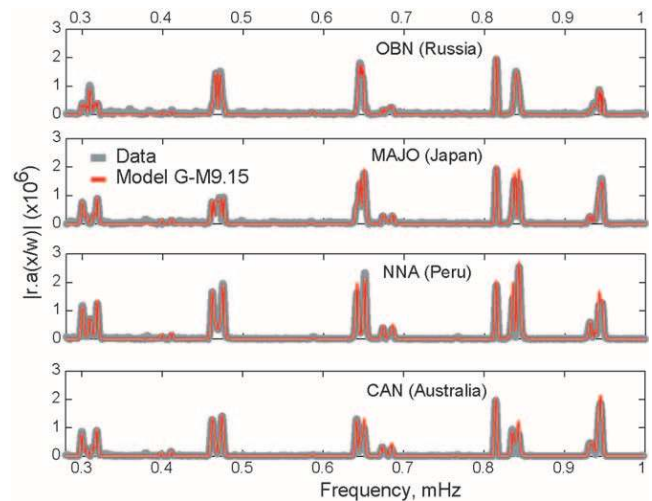


Figure 13. Comparison between normal modes data (thick line) and geodetic model G-M9.15 synthetics at four stations: OBN (Obninsk, Russia), MAJO (Matsushiro, Japan), NNA (Nana, Peru), and CAN (Canberra, Australia).

of the slip distribution would improve the fit even further, but that is not within the scope of this study.

The static estimates are computed as the average displacement in the unfiltered synthetic between 2000 and 4000 sec. In this time window, the first-orbit surface waves have passed, but the second-orbit waves have not yet arrived. In general, the waves in this time window have amplitudes much smaller than 1 mm at the location of the very-far-field (>1100 km) GPS sites, so this method can estimate displace-

ments larger than 1 mm accurately (Fig. 15). The static displacement of model G-M9.15 is consistent with the very-far-field coseismic displacements as recorded by the IGS network (Vigny *et al.*, 2005), yielding a reduced chi-square of only 0.73. Model G-M9.15 fits remarkably well data from stations in India, the Philippines, and China.

Consistency with the Tsunami Height Recorded by JASON and TOPEX

We have compared the tsunami predicted from our coseismic model G-M9.15 with the measurements of the tsunami height recorded by the satellite altimeters JASON and TOPEX/Poseidon (Fig. 16). The amplitude of the mesoscale oceanographic component is negligible in view of the sea level anomaly (Le Traon *et al.*, 1998) computed for 26 December or from the modeling of a global sea circulation (Song *et al.*, 2005), and was therefore not corrected. The simulation was computed from a finite-difference scheme based on a shallow-water approximation (Hebert *et al.*, 2001; Sladen and Hébert, 2005). The bathymetry was taken from ETOPO 2' (Smith and Sandwell, 1997). The tsunami-genic source considered here is the deformation of the seafloor computed from model G-M9.15, taking into account both the vertical and horizontal static displacements generated on a grid covering the whole rupture with the same resolution as ETOPO 2'. For simplicity we have ignored here the rupture kinematics. Our tests have shown that it has only a second-order effect on the predicted tsunami wave. The model predicts reasonably well the amplitude and wavelength of the tsunami as measured by TOPEX/Poseidon and JASON. The model fails in reproducing the trough visible at about 118–120 min (see JASON profile in Fig. 16). This trough is due to reflected waves from Aceh tip and is difficult to reproduce because we do not include runup and inundation in our modeling (E. Geist, personal comm., 2006). Modeling of the tide gauge records yields results that conflict with the inference of delayed, or slow slip, event beneath the Andaman Islands (Singh *et al.*, 2006; Fujii and Satake, 2007). Given this and the good fit of our model to the TOPEX/Poseidon measurements, we think that there is no need for more coseismic slip beneath the Andaman Islands than in our coseismic model G-M9.15. We did not compare our tsunami model with the tide gauge measurements, because modeling these data would require better knowledge of the shallow bathymetry near each station. We do note, however, that our tsunamigenic source is close to that obtained by Fujii and Satake (2007) from the joint inversion of the satellite and tide gauge data.

Postseismic Slip Model

Based on the discussion in the previous section, model G-M9.15 seems to represent coseismic displacements satisfactorily, with minimum residuals at the near-field sites that were measured 20 to 40 days after the mainshock. These

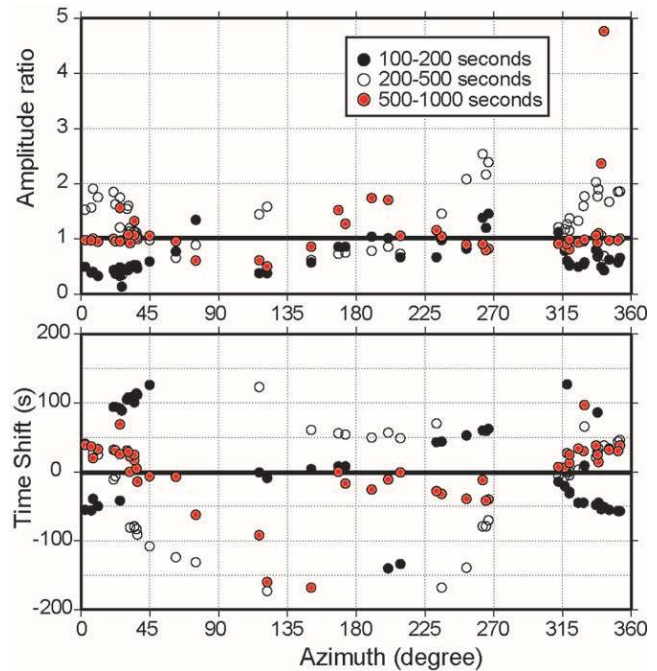


Figure 14. Misfit between seismic amplitude (top) and time shift (bottom) data and geodetic model G-M9.15 synthetics for three pass bands: 100–200 sec, 200 to 500 sec, and 500–1000 sec.

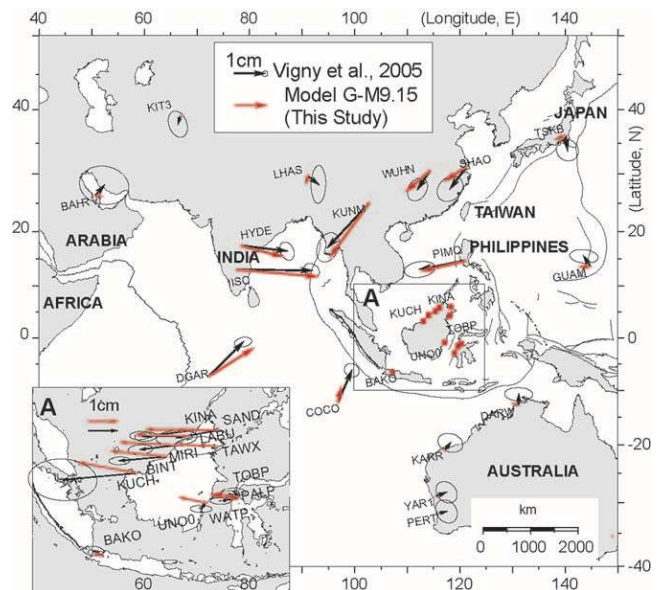


Figure 15. Comparison of the very-far-field GPS (Vigny *et al.*, 2005) and predicted displacements of model G-M9.15 computed by SEM between 2000 and 4000 sec. This model accounts for 3D structure (model Crust 2.0 [Bassin *et al.*, 2000]), ellipticity, gravity, rotation, topography, and ocean load.

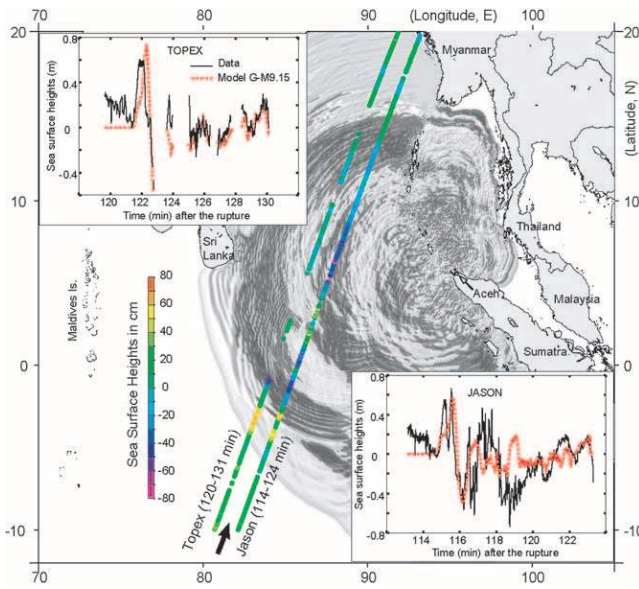


Figure 16. Sea surface heights observed by the JASON and TOPEX-Poseidon satellites compared with numerical simulations of the tsunami generated by the coseismic model G-M9.15 (dotted lines).

residuals probably reflect primarily postseismic deformation. On the other hand, model G-M9.22 shows that it is possible to account for all near-field data with an elastic dislocation model. This suggests that most of the postseismic deformation can probably be modeled as afterslip along the plate interface. In this section, we estimate more precisely the evolution and pattern of afterslip required to fit the geodetic data.

Evolution of Afterslip Derived from the CGPS Time Series

We used information from time series at four CGPS sites (reported in Fig. 3). The CGPS stations at Sampali (SAMP), in Indonesia, and on the island of Phuket (PHKT), Thailand, were already operating when the earthquake happened and thus provide the most complete records. Two CGPS stations were deployed about 50 days after the earthquake by Caltech's Tectonics Observatory as a part of the Sumatran GPS Array (SuGAR). One was installed in Lewak (LEWK), north

Simeulue, and one in Ujung Muloh (UMLH), on the western coast of Sumatra (Fig. 3a).

We have modeled the time series from these four stations using the analytical function proposed by Perfettini and Avouac (2004a, 2004b), which describes postseismic slip resulting from afterslip governed by brittle creep (that is, rate-strengthening friction) and accounts for interseismic re-loading. The displacement $U(t)$ at a given station follows the law:

$$U(t) = \beta V_0 t_r \log \left[1 + \frac{V_+}{V_0} (\exp(t/t_r) - 1) \right] \quad (3)$$

where β is the geometric factor relating the displacement $U(t)$ at the stations with slip along the plate interface, V_0 is the long-term slip velocity, V_+ is the sliding velocity of the brittle creep fault zone (BCFZ) immediately after the earthquake, and t_r is the relaxation time. For a t_r of 98 days, all the time series are fit well (Fig. 17). Thus, the evolution of postseismic displacements seems consistent with rate-strengthening frictional sliding along the plate interface. This model was then used to forecast the cumulative displacement at SAMP, PHKT, UMLH, and LEWK for any time after the earthquake. We can, in particular, predict displacements at UMLH and LEWK before their installation.

Spatial Distribution of Afterslip

We first analyzed the postseismic displacements over the first 5 days reported from the 19 CGPS stations in Thailand from Vigny *et al.* (2005) and SAMP (Table 4 in the electronic edition of BSSA). The best-fitting model, P-M8.38, yields a minimum reduced chi-square χ_r^2 of 1.80 (Table 4, Fig. 18). The released moment is M_0 0.48×10^{22} N m ($\sim M_w$ 8.38).

If we now invert the 30 first days (average time of the postseismic displacement included in the near-field residual) of cumulative postseismic displacements measured at SAMP, PHKT, UMLH, LEWK, Bangkok, and Singapore, model P-M8.64 yields a minimum χ_r^2 of 0.50 (Fig. 19) and the moment released M_0 1.18×10^{22} N m ($\sim M_w$ 8.64). The two models show a similar pattern, with slip concentrated around the downdip end of the area that ruptured during the earthquake. Both models also show a dominant patch of slip lo-

Table 4

Postseismic Model Parameters for the Inversion of 5-Days Postseismic Displacements (Table 4 in the Electronic Edition of BSSA) in the Far-Field (FF), 30-Days Postseismic Displacements (Table 5 in the Electronic Edition of BSSA) and for the Inversion of the Near-Field (NF) Residuals of Model G-M9.15 Together with 30-Days Postseismic Displacements

Name	Data Used	M_w	M_0 (10^{22} N m)	χ_r^2	Weighted Root Mean Square	Smooth
P-M8.38	5 days FF	8.38	0.48	1.80	0.23	13
P-M8.64	30 days FF	8.64	1.18	0.50	0.01	20
P-M8.82	Residuals in the NF of G-M9.15 and 30-days FF	8.82	2.44	1.51	0.8	32

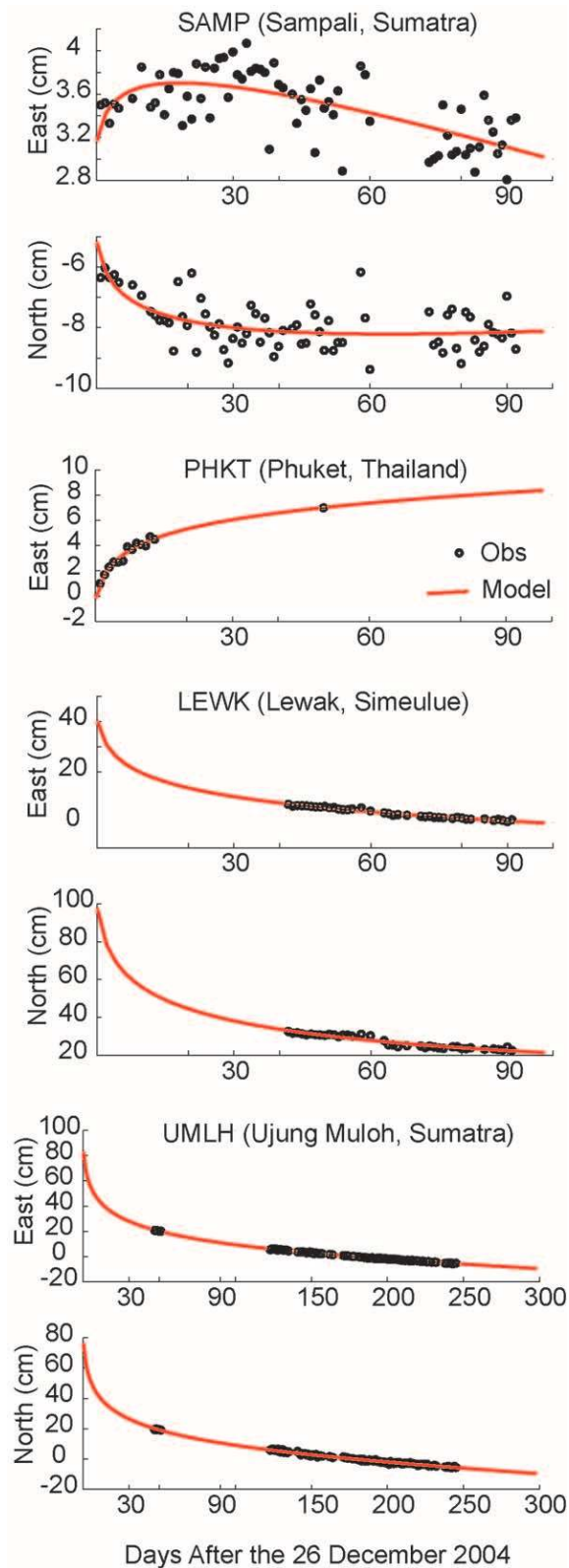


Figure 17. CGPS time series and best-fitting analytical function corresponding to frictional afterslip (Perfetti and Avouac, 2004a). The relaxation time was determined from the best fit to Sampali (SAMP) and Phuket (PHKT) time series and applied to fit the Ujung Muloh (UMLH) and Lewak (LEWK) time series.

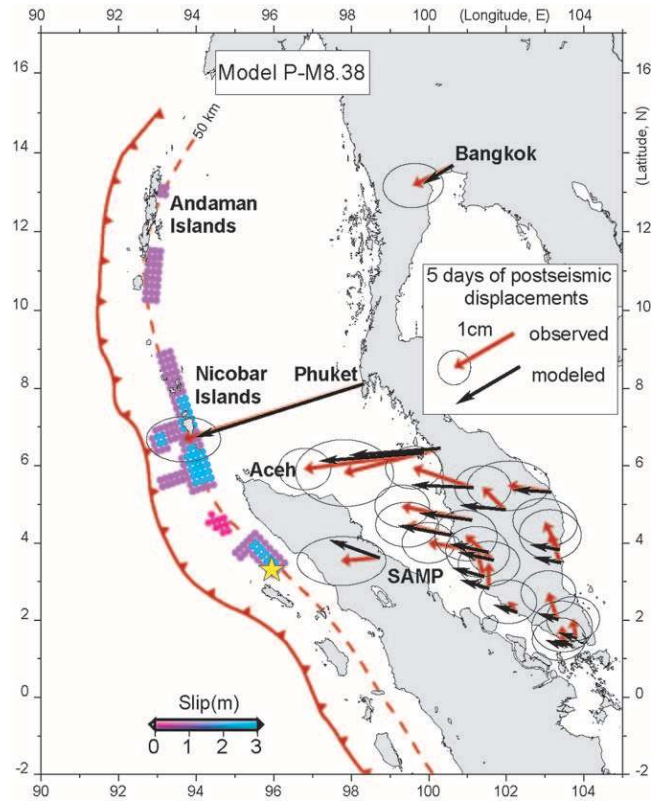


Figure 18. Inversion of the first 5 days of postseismic horizontal deformations (model P-M8.38) recorded at CGPS sites in Thailand, Malaysia, and at SAMP (Indonesia). The GPS velocities are represented with their 95% confidence ellipses.

cated southwest of Great Nicobar Island slips about 3 m after 5 days and more than 6 m after a month. The resolution of the postseismic slip is lost in the Andaman Islands, where no significant slip appears. This is due to the lack of observations there. Because of the sparse data set and the lack of data in the near field, these models are obviously not well constrained. In addition these models fail to explain the residual displacement in the near field estimated from subtracting the predictions of the coseismic model G-M9.15 from the observed displacements. This is particularly true in the Andaman Islands where the residuals are large while the postseismic models predict very little afterslip.

To refine the spatial resolution of the postseismic slip models, we have inverted all the near-field residuals displacements of model G-M9.15 together with the 30 days cumulative postseismic displacements of the six CGPS stations cited previously. The obtained model, P-M8.82 (Fig. 20) corresponds to a moment of $M_0 2.44 \times 10^{22}$ N m ($\sim M_w 8.82$), which is 35% as large as the coseismic moment, a value equivalent to the difference of moment between models G-M9.22 and G-M9.15. The reduced chi-square χ_r^2 of the model is 1.51. Afterslip is concentrated along the downdip end of the rupture, except near the extremities of the coseismic rupture (Fig. 20). Significant af-

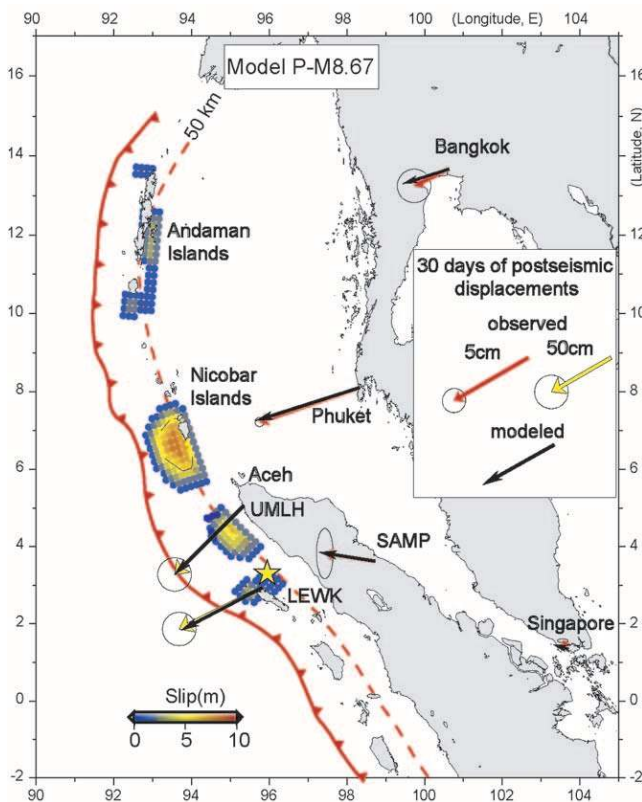


Figure 19. Inversion of the first month cumulated postseismic horizontal displacements recorded at Sampali (SAMP), Ujung Muloh (UMLH), Lewak (LEWK), Phuket, Bangkok, and Singapore (model P-M8.67). Note the change of scale between GPS velocities at UMLH and LEWK and velocities at SAMP, Phuket, Bangkok, and Singapore. Details are listed in Table 4.

terslip appears to have occurred updip of the ruptured patch near Simeulue Island. Beneath the Andaman Islands the model yields up to 10 m of afterslip, distributed along the entire megathrust from the trench to a depth of about 50 km.

Figure 21 shows the latitudinal variation of the moment released by afterslip over the first 5 days and 30 days following the earthquake, as deduced from models P-M8.38 and P-M8.82. We also show the moment released by aftershocks over the first 30 days. It shows three major peaks that seem to be correlated with the three major peaks in the distribution of coseismic moment. The total moment released by the aftershocks is about 0.016×10^{22} N m, less than 1% of the moment needed to account for postseismic displacements over the same period, indicating that postseismic deformation was almost completely aseismic.

Discussion

The model that best fits the geodetic measurements recorded within the first day of the 2004 earthquake is G-M9.15 (Fig. 9). This model is consistent with seismological,

tsunami, and T-wave observations. We deduce that the seismic rupture must have propagated as far as 15° N. The latitudinal distribution of moment in the model has three distinct peaks. This pattern is consistent with latitudinal variations in energy released by T waves and high-frequency diffracted seismic waves (Fig. 10). The general pattern in the model is a gradual northward decrease in slip. The fact that this mimics the northward decrease of the convergence rate across the plate boundary suggests that this pattern might be a characteristic feature of the large ruptures along this stretch of the megathrust.

Although our data place only low constraints on slip near the trench, it seems that the coseismic rupture didn't reach to the trench everywhere. This inference is based on the slip distribution obtained from the inversion of the geodetic data and the consistency of that model with the amplitude of the deep-sea tsunami wave. Possibly that would reflect the effect of the poorly lithified sediments at the toe of the accretionary prism on the rheology of the plate interface, which would have inhibited the propagation of the seismic rupture due to a rate-strengthening friction mechanism (Byrne *et al.*, 1988; Scholz, 1998). If this is so, one would expect afterslip on the megathrust proximal to the trench in response to stresses induced by the coseismic rupture (Marone *et al.*, 1991).

A model of frictional afterslip explains to first order the evolution of postseismic deformation. Within 40 days of the earthquake, postseismic moment release equaled about 35% of the coseismic moment, the equivalent of an M_w 8.82 earthquake (Fig. 20). The ratio of coseismic to postseismic slip is higher than this average north of 11° N. In fact, afterslip in this portion of the megathrust in the month following the earthquake was larger than the coseismic slip (Fig. 21). Perhaps this is evidence that the rheology of the megathrust there is strongly influenced by subduction of the exceptionally thick sedimentary sequence of the Bengal fan (Fig. 2). Although its spatial distribution is poorly resolved, afterslip seems to have occurred over about the same width of the megathrust as coseismic slip (compare Figs. 9 and 20).

Where resolution is best, near the southern terminus of the rupture (Fig. 4), we can resolve afterslip updip of the coseismic patch (compare Figs. 9 and 20). Otherwise, our data and analysis provide few constraints on slip near the trench. Hence, we cannot exclude the possibility that afterslip updip of the coseismic rupture may have been an ubiquitous phenomenon, as might be expected from the trenchward tapering of coseismic slip. Although shallow afterslip following large subduction earthquakes has been suspected for years, there are only few case studies where it has been documented (Miyazaki *et al.*, 2004; Hsu *et al.*, 2006).

At some places along the rupture, our model suggests some afterslip mostly downdip of the seismically ruptured area (Figs. 9 and 20). Deep afterslip might have occurred in the transition zone between the seismogenic zone, characterized by rate-weakening friction, and the deeper portion of the plate interface, which creeps continuously in the inter-

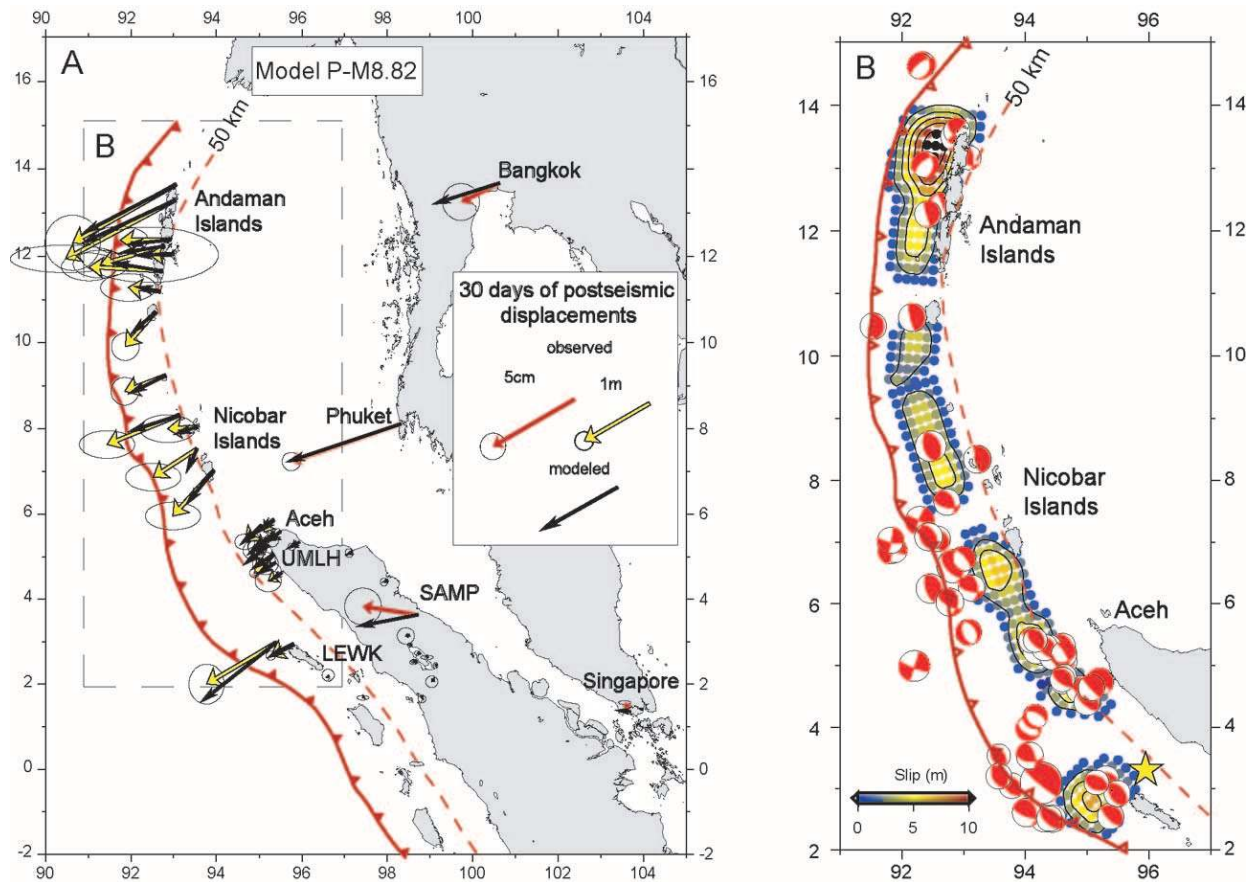


Figure 20. (a) Inversion of the residuals of G-M9.15 covering 20 to 40 days of postseismic displacements and 1-month cumulative postseismic displacements recorded at SAMP, UMLH, LEWK, Phuket, Bangkok, and Singapore (model P-M8.82). (b) Zoom on the Aceh–Nicobar–Andaman area. Harvard CMT aftershocks in the first month that follows the Sumatra–Andaman earthquake are superimposed on the postseismic slip distribution (slip contours are each 2 m).

seismic period. This transition zone seems to be delineated by background seismicity (Fig. 11) presumably because of stress accumulation at the downdip end of the locked fault zone (LFZ) in the interseismic period as observed for intra-continental megathrust (Bollinger *et al.*, 2004). The transition from the ruptured area to zone with deep afterslip occurs approximately 100–150 km from the trench. This distance compares relatively well with the 100–150 km width of the locked fault zone inferred from interseismic strain accumulation documented by geodetic measurements and coral uplift along the Batu and Mentawai segments of the Sumatra subduction zone (Prawirodirdjo *et al.*, 1997; Chlieh *et al.*, 2004a; Natawidjaja *et al.*, 2004; Simoes *et al.*, 2004). Deep afterslip has been observed for several large subduction events (Hutton *et al.*, 2001; Melbourne *et al.*, 2002; Zweck *et al.*, 2002). It has been shown in some cases to coincide with the transition zone between the LFZ and the zone creeping at the long-term slip rate (Dragert *et al.*, 1994; Mazzotti *et al.*, 2003; Chlieh *et al.*, 2004b). In most cases, even though some component of large-scale viscous relaxation might be

present, deep afterslip seems to evolve as predicted by rate-strengthening frictional sliding (Montesi, 2004; Perfettini *et al.*, 2005).

Our approach to modeling postseismic relaxation assumes that afterslip is the dominant process in the first 40 days of relaxation and neglects possible contributions of poroelasticity and viscous deformation. Poroelasticity is a near-fault process mainly visible in vertical displacements (Peltzer *et al.*, 1996). Viscous deformation of the asthenosphere is advocated to explain postseismic deformation, such as after the M_w 9.5 1960 South Chile earthquake or the M_w 9.4 1964 Alaskan earthquake (Cohen, 1999; Khazaradze *et al.*, 2002). After such giant events, viscous deformation becomes dominant over a decadal timescale but is obscured by afterslip in the early stage of relaxation as observed here. Pollitz *et al.* (2006) propose an alternative postseismic model involving a bi-viscous (Burgers body) rheology in the asthenosphere and where the downgoing Indo-Australian slab is ignored as well as the continental structure east of the megathrust. Using a laterally homoge-

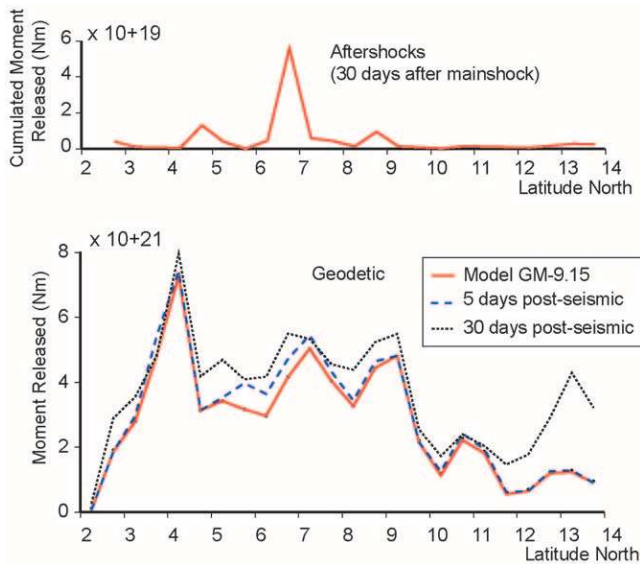


Figure 21. At the bottom, latitudinal increases of moment released by afterslip over 5-days and 30 days compared to the coseismic moment (full line) released by model G-M9.15 (cf. also Figs. 9 and 10). On top, the latitudinal variation of the moment released by aftershocks corresponds to less than 1% of the post-seismic moment released showing that nearly the entire afterslip was aseismic. Note the change of scale on the vertical axes between top and bottom.

neous viscoelastic structure, their model fits reasonably the time series of far-field GPS stations (in Thailand and at SAMP). Future investigations integrating years to decadal GPS time series, both in the near field and in the far field will certainly help to better differentiate between afterslip and viscous flow.

Because aseismic creep is thermally activated, aseismic behavior is thought to become dominant at depth and temperature might control the width of the LFZ (Hyndman and Wang, 1993; Oleskevich *et al.*, 1999). Another possibility is that the downdip end of the LFZ would coincide with the intersection of the plate interface with the forearc Moho, due to stable sliding slip along the serpentinized mantle wedge (Hyndman *et al.*, 1997). In the Sumatra–Andaman case, we discount this possibility because the forearc Moho intersects the subduction fault well updip of the bottom of the interseismic locked zone (Simoes *et al.*, 2004). The slip distribution during the great Sumatra–Andaman earthquake indicates few along-strike changes in the depth of slip. To assess how it might relate to lateral variations of the thermal structure from the Aceh area to the Andaman Islands, we estimate the depth of the 350°C isotherm, which is a commonly assumed temperature at the downdip end of the locked section at subduction zones. We find that for an average shear stress between 20 and 40 MPa on the fault and for the variety of subduction dip angles, this depth is about 40 km in the epicentral area and does not vary much along

strike from northern Sumatra to the northern Andaman Islands. This near constancy in fault-zone temperature occurs because the lower heat flow at the top of the older lithosphere in the north has longer to transmit heat to the upper plate due to the lower slip rate. Thus, it is possible that a thermally activated transition from rate weakening to rate strengthening would govern the downdip end of the seismogenic fault zone (SFZ). Given the range of plausible temperatures at this depth, it suggests that quartzo-feldspathic sediments dragged along the plate interface would govern the rheology of the plate interface.

These findings are thus consistent to the first order with the concept that the LFZ coincides approximately with the SFZ, and is bounded updip and downdip by a transition from rate-weakening to rate-strengthening friction (Tse and Rice, 1986; Scholz, 1998). Although this subduction zone can produce giant earthquakes, the large proportion of afterslip on the Sumatra subduction fault and the large regions that did not slip during this earthquake might indicate that a large fraction of the plate interface at depth shallower than about 50 km might in fact slip aseismically. Aseismic slip may be triggered by large events or may occur spontaneously as has been observed in many places (Hirose *et al.*, 1999; Dragert *et al.*, 2001) and more particularly along the Sumatra subduction zone in 1962 (Natawidjaja *et al.*, 2004). This might provide an explanation for the generally low seismic coupling found along subduction zones (Ruff and Kanamori, 1983), meaning that the seismic moment released along subduction zones in general fails to match the value estimated from the long-term slip rate along the seismogenic portion of the plate interface. If the proportion of aseismic to seismic slip during the 2004 Sumatra–Andaman earthquake is representative of the long-term average, this factor might be of the order of only 0.5 on average and even smaller in the Andaman and Nicobar area, a value consistent with the relatively low seismic activity of this segment of the subduction zone.

We estimate the repeat time of giant 2004 ruptures by dividing the rupture potency (including the postseismic contribution) by its accumulation rate. The area of the subduction interface north of the Equator to about 14° N is about 4.0×10^5 km². If we suppose a long-term normal slip rate in the range of 1 to 3 cm/yr, it yields to a potency accumulation rate of 4 to 12 km³/yr. If the slip potency is released wholly in this type of event, it would occur every 140–420 years. This estimate neglects the contribution of smaller events such as the 1881 and 1941 earthquakes and eventual spontaneous aseismic events.

Acknowledgments

The Gordon and Betty Moore Foundation and the National Science Foundation EAR0530899 supported this research. Thanks to R. W. Briggs for his helpful readings. We are grateful to the two anonymous reviewers for comments and suggestions. This is Caltech Tectonics Observatory contribution no. 31.

References

- Ammon, C. J., C. Ji, H. K. Thio, D. Robinson, S. D. Ni, V. Hjorleifsdottir, H. Kanamori, T. Lay, S. Das, D. Helmberger, G. Ichinose, J. Polet, and D. Wald (2005). Rupture process of the 2004 Sumatra–Andaman earthquake, *Science* **308**, 1133–1139.
- Banerjee, P., F. F. Pollitz, and R. Bürgmann (2005). The size and duration of the Sumatra–Andaman earthquake from far-field static offsets, *Science* **308**, 1769–1772.
- Banerjee, P., F. Pollitz, B. Nagarajan, and R. Bürgmann (2007). Coseismic slip distributions of the 26 December 2004 Sumatra–Andaman and 28 March 2005 Nias earthquakes from GPS static offsets, *Bull. Seism. Soc. Am.* **97**, no. 1A, S86–S102.
- Bassin, C., G. Laske, and G. Masters (2000). The current limits of resolution for surface wave tomography in North America, *EOS Trans. AGU* **81**, no. 48, S12A–03.
- Bettinelli, P., J. P. Avouac, M. Flouzat, F. Jouanne, L. Bollinger, P. Willis, and G. R. Chitraker (2006). Plate motion of India and interseismic strain in the Nepal Himalaya from GPS and DORIS measurements, *J. Geodesy* (in press), doi 10.1007/s00190-006-0030-3.
- Bilek, S. L. (2007). Using earthquake rupture variations along the Sumatra–Andaman subduction system to examine fault zone variations, *Bull. Seism. Soc. Am.* **97**, no. 1A, S62–S70.
- Bilham, R. (2005). A flying start, then a slow slip, *Science* **308**, 1126–1127.
- Bilham, R., R. Engdahl, N. Feldl, and S. P. Satyabala (2005). Partial and complete rupture of the Indo–Andaman plate boundary 1847–2004, *Seism. Res. Lett.* **76**, 299–311.
- Bock, Y., L. Prawirodirdjo, J. F. Genrich, C. W. Stevens, R. McCaffrey, C. Subarya, S. S. O. Puntodewo, and E. Calais (2003). Crustal motion in Indonesia from Global Positioning System measurements, *J. Geophys. Res.* **109**, B8, 2367, doi 10.1029/2001JB000324.
- Bollinger, L., J. P. Avouac, R. Cattin, and M. R. Pandey (2004). Stress buildup in the Himalaya, *J. Geophys. Res.* **109**, B11405, doi 10.1029/2003JB002911.
- Briggs, R. W., K. Sieh, A. J. Meltzner, D. Natawidjaja, J. Galetzka, B. Suwargadi, Y. J. Hsu, M. Simons, N. Hananto, I. Suprihanto, D. Prayudi, J. P. Avouac, L. Prawirodirdjo, and Y. Bock (2006). Deformation and slip along the Sunda Megathrust in the great 2005 Nias–Simeulue earthquake, *Science* **311**, 1897–1901.
- Byrne, D. E., D. M. Davis, and L. R. Sykes (1988). Loci and maximum size of thrust earthquakes and the mechanics of the shallow region of subduction zones, *Tectonics* **7**, 833–857.
- Cande, S. C., and D. V. Kent (1995). Revised calibration of the geomagnetic polarity timescale for the late Cretaceous and Cenozoic, *J. Geophys. Res.* **100**, 6093–6095.
- Catherine, J. K., V. K. Gahalaut, and V. K. Sahu (2005). Constraints on rupture of the December 26, 2004, Sumatra earthquake from far-field GPS observations, *Earth Planet. Sci. Lett.* **237**, 673–679.
- Chlieh, M., J. Avouac, K. Sieh, D. Natawidjaja, and J. Galetzka (2004a). Investigating lateral variations of interseismic strain along the Sumatran subduction zone (abstract), *EOS Trans. AGU* **85** (Fall Meet. Suppl.), T13C–1385.
- Chlieh, M., J. B. de Chabaliere, J. C. Ruegg, R. Armijo, R. Dmowska, J. Campos, and K. L. Feigl (2004b). Crustal deformation and fault slip during the seismic cycle in the North Chile subduction zone, from GPS and InSAR observations, *Geophys. J. Int.* **158**, 695–711.
- Cohen, S. C. (1999). Numerical models of crustal deformation in seismic zones, *Adv. Geophys.* **41**, 134–231.
- Curry, J. R. (2005). Tectonics and history of the Andaman Sea region, *J. Asian Earth Sci.* **25**, 187–228.
- Dahlen, T., and J. Tromp (1998). *Theoretical Global Seismology*, Princeton University Press, Princeton, New Jersey.
- de Groot-Hedlin, C. D. (2005). Estimation of the rupture length and velocity of the Great Sumatra earthquake of Dec. 26, 2004 using hydroacoustic signals, *Geophys. Res. Lett.* **32**, L11303, doi 10.1029/2005GL022695.
- Dewey, J. W., G. Choy, B. Presgrave, S. Sipkin, A. C. Tarr, H. Benz, P. Earle, and D. Wald (2007). Seismicity associated with the Sumatra–Andaman islands earthquake of December 26, 2004, *Bull. Seism. Soc. Am.* **97**, no. 1A, S25–S42.
- Dragert, H., R. D. Hyndman, G. C. Rogers, and K. Wang (1994). Current deformation and the width of the seismogenic zone of the Northern Cascadia Subduction Thrust, *J. Geophys. Res.* **99**, 653–668.
- Dragert, H., K. Wang, and T. S. James (2001). A silent slip event on the deeper Cascadia subduction interface, *Science* **292**, 1525–1527.
- Engdahl, E., R. van der Hilst, and R. Buland (1998). Global teleseismic earthquake relocation with improved travel times and procedures for depth determination, *Bull. Seism. Soc. Am.* **88**, 722–743.
- Fitch, T. J. (1972). Plate convergence, transcurrent faults and internal deformation adjacent to southeast Asia and the western Pacific, *J. Geophys. Res.* **77**, 4432–4460.
- Fujii, Y., and K. Satake (2007). Tsunami source of the 2004 Sumatra–Andaman earthquake inferred from tide gauge and satellite data, *Bull. Seism. Soc. Am.* **97**, no. 1A, S192–S207.
- Gahalaut, V. K., B. Nagarajan, J. K. Catherine, and S. Kumar (2006). Constraints on 2004 Sumatra–Andaman earthquake rupture from GPS measurements in Andaman–Nicobar Islands, *Earth Planet. Sci. Lett.* **242**, 365–374.
- Genrich, J. F., Y. Bock, R. McCaffrey, L. Prawirodirdjo, C. Stevens, S. S. O. Puntodewo, C. Subarya, and S. Wdowsky (2000). Distribution of slip at the northern Sumatran fault system, *J. Geophys. Res.* **105**, 722–743.
- Global Centroid Moment Tensor (CMT) Project catalog search, www.globalcmt.org/CMTsearch.html (last accessed April 2006).
- Gower, J. F. (2005). Jason 1 detects December 26, 2004 tsunami, *EOS Trans. AGU* **86**, 37–38.
- Gradstein, F. M., F. P. Agterberg, J. G. Ogg, J. Hardenbol, P. van Veen, J. Thierry, and Z. Huang (1994). A Mesozoic time scale, *J. Geophys. Res.* **99**, 24,051–24,074.
- Gudmundsson, O., and M. Sambridge (1998). A regionalized upper mantle (RUM) seismic model, *J. Geophys. Res.* **103**, 7121–7136.
- Guilbert, J., J. Vergoz, E. Schisselle, A. Roueff, and Y. Cansi (2005). Use of hydroacoustic and seismic arrays to observe rupture propagation and source extent of the $M_w = 9.0$ Sumatra earthquake, *Geophys. Res. Lett.* **32**, L15310, doi 10.1029/2005GL022966.
- Hashimoto, M., N. Choosakul, M. Hashizume, S. Takemoto, H. Takiguchi, Y. Fukuda, and K. Frjimori (2006). Crustal deformations associated with the great Sumatra–Andaman earthquake deduced from continuous GPS observation, *Earth Planets Space* **58**, 127–139.
- Hébert, H., P. Heinrich, F. Schindele, and A. Piatanesi (2001). Far-field simulation of tsunami propagation in the Pacific Ocean: impact on the Marquesas Islands (French Polynesia), *J. Geophys. Res.* **106**, 9161–9177.
- Hirose, H., K. Hirahara, F. Kimata, N. Fujii, and S. Miyazaki (1999). A slow thrust slip event following the two 1996 Hyuganada earthquakes beneath the Bungo Channel, southwest Japan, *Geophys. Res. Lett.* **21**, 3237–3240.
- Hsu, Y.-J., M. Simons, J. P. Avouac, K. Sieh, J. Galetzka, M. Chlieh, Y. Bock, D. H. Natawidjaja, and L. Prawirodirdjo (2006). Frictional afterslip following the M_w 8.7, 2005 Nias–Simeulue earthquake, Sumatra, *Science* **312**, 1921–1926.
- Hutton, W., C. DeMets, O. Sanchez, G. Suarez, and J. Stock (2001). Slip kinematics and dynamics during and after the 1995 October 9 $M_w = 8.0$ Colima–Jalisco earthquake, Mexico, from GPS geodetic constraints, *Geophys. J. Int.* **146**, 637–658.
- Hyndman, R. D., and K. Wang (1993). Thermal constraints on the zone of major thrust earthquake failure: the Cascadia subduction zone, *J. Geophys. Res.* **98**, 2039–2060.
- Hyndman, R. D., M. Yamano, and D. A. Oleskevich (1997). The seismogenic zone of subduction thrust faults, *The Island Arc* **6**, 244–260.
- Ishii, M., P. M. Shearer, H. Houston, and J. E. Vidale (2005). Extent, duration and speed of the 2004 Sumatra–Andaman earthquake imaged by the Hi-Net array, *Nature* **435**, 933–936.

- Jade, J., M. B. Ananda, P. Dileep Kumar, and S. Banerjee (2005). Co-seismic and post-seismic displacements in Andaman and Nicobar Islands from GPS measurements, *Curr. Sci.*, **88**, 1980–1984.
- Ji, C., D. Wald, and D. V. Helmburger (2002). Source description of the 1999 Hector Mine, California earthquake, Part I: Wavelet domain inversion theory and resolution analysis, *Bull. Seism. Soc. Am.*, **92**, 1192–1207.
- Khazaradze, G., K. Wang, J. Klotz, Y. Hu, and J. He (2002). Prolonged post-seismic deformation of the 1960 great Chile earthquake and implications for mantle rheology, *Geophys. Res. Lett.*, **29**, 2050, doi 10.1029/2002GL015986.
- Komatitsch, D., and J. Tromp (2002a). Spectral-element simulations of global seismic wave propagation. I. Validation, *Geophys. J. Int.*, **149**, 390–412.
- Komatitsch, D., and J. Tromp (2002b). Spectral-element simulations of global seismic wave propagation. II. Three-dimensional models, oceans, rotation and self-gravitation, *Geophys. J. Int.*, **150**, 303–318.
- Konca, A. O., V. Hjorleifsdottir, T. Song, J.-P. Avouac, D. V. Don Helmburger, C. Ji, K. Sieh, R. Briggs, and A. Meltzner (2007). Rupture kinematics of the 2005, Mw 8.6, Nias-Simeulue earthquake from the joint inversion of seismic and geodetic data, *Bull. Seism. Soc. Am.*, **97**, no. 1A, S307–S322.
- Kreemer, C., G. Blewitt, W. C. Hammond, and H. P. Plag (2006a). Global deformation from the great 2004 Sumatra-Andaman Earthquake observed by GPS: implications for rupture process and global reference frame, *Earth Planets Space*, **58**, 141–148.
- Kreemer, C., G. Blewitt, and F. Maerten (2006b). Co- and postseismic deformation of the 28 March 2005 Nias Mw 8.7 earthquake from continuous GPS data, *Geophys. Res. Lett.*, **33**, L07307, doi 10.1029/2005GL025566.
- Krüger, F., and M. Ohrnberger (2005). Tracking the rupture of the Mw = 9.3 Sumatra earthquake over 1,150 km at teleseismic distance, *Nature*, **435**, 937–939.
- Lay, T., H. Kanamori, C. J. Ammon, M. Nettles, S. N. Ward, R. C. Aster, S. L. Beck, S. L. Bilek, M. R. Brudzinski, R. Butler, H. R. DeShon, G. Ekstrom, K. Satake, and S. Sipkin (2005). The great Sumatra-Andaman earthquake of 26 December 2004, *Science*, **308**, 1127–1133.
- Le Traon, P. Y., F. Nadal, and N. Ducet (1998). An improved mapping method of multisatellite altimeter data, *J. Atmos. Oceanic Technol.*, **15**, 522–533.
- Marone, C., C. Scholtz, and R. Bilham (1991). On the mechanics of earthquake afterslip, *J. Geophys. Res.*, **96**, 8441–8452.
- Mazzotti, S., H. Dragert, J. Henton, M. Schmidt, R. Hyndman, T. James, Y. Lu, and M. Craymer (2003). Current tectonics of northern Cascadia from a decade of GPS measurements, *J. Geophys. Res.*, **108**, 2554, doi 10.1029/2003JB002653.
- McCaffrey, R., P. Zwick, Y. Bock, L. Prawirodirdjo, J. Genrich, C. Stevens, S. Puntodewo, and C. Subarya (2000). Strain partitioning during oblique plate convergence in northern Sumatra: geodetic observations and numerical modeling, *J. Geophys. Res.*, **105**, 28,363–28,375.
- Melbourne, T. I., F. H. Webb, J. M. Stock, and C. Reigber (2002). Rapid postseismic transients in subduction zones from continuous GPS, *J. Geophys. Res.*, **107**, 2241, doi 10.1029/2001JB000555.
- Meltzner, A. J., K. Sieh, M. Abrams, D. C. Agnew, K. W. Hudnut, J.-P. Avouac, and D. H. Natawidjaja (2006). Uplift and subsidence associated with the great Aceh-Andaman earthquake of 2004, *J. Geophys. Res.*, **111**, B02407, doi 10.1029/2005JB003891.
- Merrifield, M. A., Y. L. Firing, T. Aarup, W. Agricole, G. Brundrit, D. Chang-Seng, R. Farre, B. Kilonsky, W. Knight, L. Kong, C. Magori, P. Manurung, C. McCreery, W. Mitchell, S. Pillay, F. Schindele, F. Shillington, L. Testut, E. M. S. Wijeratne, P. Caldwell, J. Jardin, S. Nakahara, F.-Y. Porter, and N. Turetsky (2005). Tide gauge observations of the Indian Ocean tsunami, December 26, 2004, *Geophys. Res. Lett.*, **32**, L09603, doi 10.1029/2005GL022610.
- Michel, G. W., Y. Q. Yu, S. Y. Zhu, C. Reigber, M. Becker, E. Reinhard, W. Simons, B. Ambrosius, C. Vigny, N. Chamot-Rooke, X. Le Pichon, P. Morgan, and S. Matheussen (2001). Crustal motion and block behaviour in SE-Asia from GPS measurements, *Earth Planet. Sci. Lett.*, **187**, 239–244.
- Miyazaki, S., P. Segall, J. Fukuda, and T. Kato (2004). Space time distribution of afterslip following the 2003 Tokachi-oki earthquake: Implications for variations in fault zone frictional properties, *Geophys. Res. Lett.*, **31**, L06623, doi 10.1029/2003GL019410.
- Montési, L. G. J. (2004). Controls of shear zone rheology and tectonic loading on postseismic creep, *J. Geophys. Res.*, **109**, B10404, doi 10.1029/2003JB002925.
- Natawidjaja, D., K. Sieh, M. Chlieh, J. Galetzka, B. Suwargadi, H. Cheng, R. L. Edwards, J.-P. Avouac, and S. Ward (2006). The giant Sumatran megathrust ruptures of 1797 and 1833: Paleoseismic evidence from coral microatolls, *J. Geophys. Res.*, **111**, B06403, doi 10.1029/2005JB004025.
- Natawidjaja, D., K. Sieh, S. Ward, H. Cheng, R. L. Edwards, J. Galetzka, and B. Suwargadi (2004). Paleogeodetic records of seismic and aseismic subduction from central Sumatran microatolls, Indonesia, *J. Geophys. Res.*, **109**, B04306, doi 10.1029/2003JB0002398.
- Neetu, S., I. Suresh, R. Shankar, D. Shankar, S. S. C. Sheno, S. R. Shetye, D. Sundar, and B. Nagarajan (2005). Comment on “The great Sumatra-Andaman earthquake of 26 December 2004,” *Science*, **310**, 5753, doi 10.1126/science.1118950.
- Newcomb, K., and W. McCann (1987). Seismic history and seismotectonics of the Sunda Arc, *J. Geophys. Res.*, **92**, 421–439.
- Ni, S., H. Kanamori, and D. Helmburger (2005). Energy radiation from the Sumatra earthquake, *Nature*, **434**, 582.
- Ohta, Y., I. Meilano, T. Sagiya, F. Kimata, and K. Hirahara (2006). Large surface wave of the 2004 Sumatra-Andaman earthquake captured by the very long baseline kinematic analysis of 1-Hz GPS data, *Earth Planets Space*, **58**, 153–157.
- Oleskevich, D. A., R. D. Hyndman, and K. Wang (1999). The updip and downdip limits to great subduction earthquakes: thermal and structural models of Cascadia, south Alaska, SW Japan, and Chile, *J. Geophys. Res.*, **104**, 14,965–14,991.
- Ortiz, M., and R. Bilham (2003). Source area and rupture parameters of the 31 December 1881 M-w = 7.9 Car Nicobar earthquake estimated from tsunamis recorded in the Bay of Bengal, *J. Geophys. Res.*, **108**.
- Park, J., and F. Gilbert (1986). Coupled free oscillations of an aspherical, dissipative, rotating earth—Galerkin theory, *J. Geophys. Res.*, **91**, 7241–7260.
- Park, J., T. R. A. Song, J. Tromp, E. Okal, S. Stein, G. Roullet, E. Clevede, G. Laske, H. Kanamori, P. Davis, J. Berger, C. Braitenberg, M. Van Camp, X. Lei, H. P. Sun, H. Z. Xu, and S. Rosat (2005). Earth’s free oscillations excited by the 26 December 2004 Sumatra-Andaman earthquake, *Science*, **308**, 1139–1144.
- Paul, J., R. Burgmann, V. K. Gaur, R. Bilham, K. M. Larson, M. B. Ananda, S. Jade, M. Mukal, T. S. Anupama, G. Satyal, and D. Kumar (2001). The motion and active deformation of India, *Geophys. Res. Lett.*, **28**, 647–650.
- Peltzer, G., P. Rosen, F. Rogez, and K. Hudnut (1996). Postseismic rebound in fault step-overs caused by pore fluid flow, *Science*, **273**, 1202–1204.
- Perfettini, H., and J.-P. Avouac (2004a). Postseismic relaxation driven by brittle creep: a possible mechanism to reconcile geodetic measurements and the decay rate of aftershocks, application to the Chi-Chi earthquake, Taiwan, *J. Geophys. Res.*, **109**, B02304, doi 10.1029/2003JB002488.
- Perfettini, H., and J.-P. Avouac (2004b). Stress transfer and strain rate variations during the seismic cycle, *J. Geophys. Res.*, **109**, B06402, doi 10.1029/2003JB002917.
- Perfettini, H., J.-P. Avouac, and J.-C. Ruegg (2005). Geodetic displacements and aftershocks following the 2001 Mw = 8.4 Peru earthquake: implications for the mechanics of the earthquake cycle along subduction zones, *J. Geophys. Res.*, **110**, B09404, doi 10.1029/2004JB003522.
- Pollitz, F. F., P. Banerjee, R. Bürgmann, M. Hashimoto, and N. Choosakul (2006). Stress changes along the Sunda trench following the 26 December 2004 Sumatra-Andaman and 28 March 2005 Nias earthquakes, *Geophys. Res. Lett.*, **33**, L06309, doi 10.1029/2005GL024558.
- Prawirodirdjo, L., Y. Bock, J. Genrich, S. S. O. Puntodewo, J. Rais, C.

- Subarya, and S. Sutisna (2000). One century of tectonic deformation along the Sumatran Fault from triangulation and GPS surveys, *J. Geophys. Res.* **105**, 28,343–28,362.
- Prawirodirdjo, L., Y. Bock, R. McCaffrey, J. Genrich, E. Calais, C. Stevens, S. S. O. Puntodewo, C. Subarya, J. Rais, P. Zwick, and Fauzi (1997). Geodetic observations of interseismic strain segmentation at the Sumatra subduction zone, *Geophys. Res. Lett.* **24**, 2601–2604.
- Ritsema, J., H. J. van Heijst, and J. H. Woodhouse (1999). Complex shear wave velocity structure imaged beneath Africa and Iceland, *Science* **286**, 1925–1928.
- Rivera, L., K. Sieh, D. Helmberger, and D. Natawidjaja (2002). A comparative study of the Sumatran subduction-zone earthquakes of 1935 and 1984, *Bull. Seism. Soc. Am.* **92**, 1721–1736.
- Ruff, L., and H. Kanamori (1983). Seismic coupling and uncoupling at subduction zones, *Tectonophysics* **99**, 99–117.
- Scholz, C. H. (1998). Earthquakes and friction laws, *Nature* **391**, 37–42.
- Sieh, K., and D. Natawidjaja (2000). Neotectonics of the Sumatran fault, Indonesia, *J. Geophys. Res.* **105**, 28,295–28,326.
- Sieh, K., D. Natawidjaja, M. Chlieh, J. Galetzka, and J.-P. Avouac (2004). The giant subduction earthquakes of 1797 and 1833, West Sumatra: characteristic couplets, uncharacteristic slip (abstract), *EOS Trans. AGU* **85** (Fall Meet. Suppl.), T12B-04.
- Simoes, M., J. P. Avouac, R. Cattin, and P. Henry (2004). The Sumatra subduction zone: a case for a locked fault zone extending into the mantle, *J. Geophys. Res.* **109**, B10402, doi 10.1029/2003JB002958.
- Singh, S. K., M. Ortiz, H. K. Gupta, and D. G. A. Ramadass (2006). Slow slip below Port Blair, Andaman, during the great Sumatra–Andaman earthquake of 26 December 2004, *Geophys. Res. Lett.* **33**, L03313, doi 10.1029/2005GL025025.
- Sladen, A., and H. Hébert (2005). Inversion of satellite altimetry data to recover the Sumatra 2004 earthquake slip distribution (abstract), *EOS Trans. AGU* **86** (Fall Meet. Suppl.), U22A-07.
- Smith, W., and D. Sandwell (1997). Global sea floor topography from satellite altimetry and ship depth soundings, *Science* **277**, 1956–1962.
- Socquet, A., C. Vigny, N. Chamot-Rooke, W. Simons, C. Rangin, and B. Ambrosius (2006). India and Sunda Plates motion and deformation along their boundary in Myanmar determined by GPS, *J. Geophys. Res.* **111**, B05406, doi 10.1029/2005JB003877.
- Song, Y. T., C. Ji, L. L. Fu, V. Zlotnicki, C. K. Shum, Y. C. Yi, and V. Hjorleifsdottir (2005). The 26 December 2004 tsunami source estimated from satellite radar altimetry and seismic waves, *Geophys. Res. Lett.* **32**, L20601, doi 10.1029/2005GL023683.
- Stein, S., and E. A. Okal (2005). Speed and size of the Sumatra earthquake, *Nature* **434**, 581–582.
- Subarya, C., M. Chlieh, L. Prawirodirdjo, J. P. Avouac, Y. Bock, K. Sieh, A. J. Meltzner, D. H. Natawidjaja, and R. McCaffrey (2006). Plate-boundary deformation associated with the great Sumatra–Andaman earthquake, *Nature* **440**, 46–51.
- Titov, V., A. B. Rabinovich, H. O. Mofjeld, R. E. Thomson, and F. I. Gonzalez (2005). The global reach of the 26 December 2004 Sumatra tsunami, *Science* **309**, 2045–2048.
- Tobita, M., H. Suito, T. Imakiire, M. Kato, S. Fujiwara, and M. Murakami (2006). Outline of vertical displacement of the 2004 and 2005 Sumatra earthquakes revealed by satellite radar imagery, *Earth Planets Space* **58**, e1–e4.
- Tsai, V. C., M. Nettles, G. Ekstrom, and A. M. Dziewonski (2005). Multiple CMT source analysis of the 2004 Sumatra earthquake, *Geophys. Res. Lett.* **32**, L17304, doi 10.1029/2005GL023813.
- Tse, S. T., and J. R. Rice (1986). Crustal earthquake instability in relation to the depth variation of frictional slip properties, *J. Geophys. Res.* **91**, 9452–9472.
- Vallée, M. (2007). Rupture properties of the giant Sumatra earthquake imaged by empirical Green function analysis, *Bull. Seism. Soc. Am.* **97**, no. 1A, S103–S114.
- Vigny, C., W. J. F. Simons, S. Abu, R. Bamphenyu, C. Satirapod, N. Choo-sakul, C. Subarya, A. Socquet, K. Omar, H. Z. Abidin, and B. A. C. Ambrosius (2005). Insight into the 2004 Sumatra–Andaman earthquake from GPS measurements in southeast Asia, *Nature* **436**, 201–206.
- Xie, X., and Z. X. Yao (1989). A generalized reflection-transmission coefficient matrix method to calculate static displacement field of a dislocation source in a stratified half space, *Chinese J. Geophys.* **32**, 191–205.
- Zachariasen, J., K. Sieh, F. W. Taylor, R. L. Edwards, and W. S. Hantoro (1999). Submergence and uplift associated with the giant 1833 Sumatran subduction earthquake: evidence from coral microatolls, *J. Geophys. Res.* **104**, 895–919.
- Zweck, C., J. T. Freymueller, and S. C. Cohen (2002). Three-dimensional elastic dislocation model of the postseismic response to the 1964 Alaska earthquake, *J. Geophys. Res.* **107**, 10.1029–10.1042.

Tectonics Observatory
Division of Geological and Planetary Sciences
California Institute of Technology
Pasadena, California 91125
(M.C., J.-P.A., V.H., T.-R.A.S., C.J., K.S., J.G.)

Laboratoire de Détection et de Géophysique
CEA, 91680 Bruyère-le-Châtel, France
(A.S., H.H.)

Scripps Institution of Oceanography
University of California San Diego
La Jolla, California 92093
(L.P., Y.B.)

Manuscript received 16 February 2006.